
EXPLAINABLE MULTIMODAL REGRESSION VIA INFORMATION DECOMPOSITION

PREPRINT

Zhaozhao Ma^{*,†}

^{*}Zhejiang University

[†]Georgia Institute of Technology

zhaozhaoma@gatech.edu

Shujian Yu^{‡,§}

[‡]Vrije Universiteit Amsterdam

[§]UiT - The Arctic University of Norway

s.yu3@vu.nl

ABSTRACT

Multimodal regression aims to predict a continuous target from heterogeneous input sources and typically relies on fusion strategies such as early or late fusion. However, existing methods lack principled tools to disentangle and quantify the individual contributions of each modality and their interactions, limiting the interpretability of multimodal fusion. We propose a novel multimodal regression framework grounded in Partial Information Decomposition (PID), which decomposes modality-specific representations into unique, redundant, and synergistic components. The basic PID framework is inherently underdetermined. To resolve this, we introduce inductive bias by enforcing Gaussianity in the joint distribution of latent representations and the transformed response variable (after inverse normal transformation), thereby enabling analytical computation of the PID terms. Additionally, we derive a closed-form conditional independence regularizer to promote the isolation of unique information within each modality. Experiments on six real-world datasets, including a case study on large-scale brain age prediction from multimodal neuroimaging data, demonstrate that our framework outperforms state-of-the-art methods in both predictive accuracy and interpretability, while also enabling informed modality selection for efficient inference. Implementation is available at **PIDReg**.

1 Introduction

Multimodal regression has become increasingly important due to its ability to effectively integrate heterogeneous data sources to predict a continuous target, and has found applications across a wide range of domains. In healthcare diagnostics, for example, it leverages medical imaging and clinical text data to predict patient outcomes such as survival time and disease severity scores [Soenksen et al., 2022]. In sentiment analysis, models combine audio, visual, and textual information to assess human emotions and opinions more accurately [Soleymani et al., 2017]. To support such tasks, various multimodal fusion paradigms have been proposed, ranging from widely used attention-based mechanisms [Hori et al., 2017, Tsai et al., 2019] to more recent methods grounded in the information bottleneck (IB) principle [Tishby et al., 2000, Mai et al., 2022]. Despite its performance gains, multimodal regression often faces substantial interpretability challenges, particularly at the modality level. For example, in sentiment prediction, several critical questions arise: Does the audio modality contribute more predictive power than text? Do audio and video modalities create a synergistic effect that enhances the final decision, or are they largely redundant, such that a single modality is sufficient for reliable predictions? The lack of clarity regarding the specific contributions and interactions of modalities undermines model trustworthiness, transparency, and practical applicability in real-world settings [Das and Rad, 2020, Tsankova et al., 2015].

The partial information decomposition (PID) framework [Kraskov et al., 2004, Kolchinsky, 2022, Williams and Beer, 2010], originally developed in neuroscience, offers a formal approach to quantify how two random variables x_1 and x_2 interact with a third variable y by decomposing the mutual information $I(x_1, x_2; y)$ between (x_1, x_2) and y into four non-negative components: two unique information terms, U_1 and U_2 , which capture the individual contributions of x_1 and x_2 ; a synergy term S , representing information that emerges only from the joint knowledge of both variables; and a redundancy term R , which reflects information about y that is attainable by either x_1 or x_2 . This elegant decomposition

makes PID a promising tool for analyzing how multimodal interactions contribute to predictive outcomes. However, its application in multimodal learning remains limited and underexplored [Liang et al., 2023, Xin et al., 2025], largely due to the underdetermined nature of the decomposition, which leads to intractable optimization when dealing with continuous and high-dimensional variables.

This work presents **PIDReg**, a novel multimodal regression framework that enables the computation of **PID** and seamlessly integrates it into an end-to-end learning process. The key idea is to enforce the joint distribution of the learned modality-specific representations and the target response variable (after the inverse normal transformation [Conover, 1999]) to follow a multivariate Gaussian, thereby enabling an analytical PID solution even in high-dimensional settings. To support this, we introduce two regularization terms: one that promotes Gaussianity and another that encourages the uniqueness of information captured by each modality-specific encoder. Both are formulated using the recently re-emerged Cauchy–Schwarz (CS) divergence [Yu et al., 2025, 2024a]. To summarize:

1. We propose a generic PID-based multimodal regression framework that ensures interpretability by revealing the contributions of individual modalities and their high-order interactions to the output.
2. We develop an analytically tractable optimization scheme for PIDReg for continuous and high-dimensional variables, incorporating Gaussianity enforcement via the Shapiro–Wilk test [Shapiro and Wilk, 1965] and a CS divergence-based conditional independence regularization.
3. Extensive experiments on six real-world applications from diverse domains, including healthcare, physics, affective computing, and robotics, and covering both univariate and multivariate prediction tasks, demonstrate that PIDReg outperforms six state-of-the-art methods in terms of both predictive accuracy and interpretability.

2 Related Work

2.1 Fusion Strategies in Multimodal Learning

Various fusion paradigms have been proposed for multimodal learning [Li and Tang, 2024]. Early fusion, also known as feature-level fusion, combines modalities either by concatenating raw features [Ortega et al., 2019] or integrating modality-specific embeddings [Mai et al., 2022, Tsai et al., 2019, Zadeh et al., 2017]. Late fusion, or decision-level fusion, trains separate models per modality and aggregates their predictions [Huang et al., 2020]. In addition, hybrid fusion strategies combine the merits of early and late fusion to exploit their complementary advantages [Hemker et al., 2024].

Among these, feature-level fusion is widely used in multimodal learning, as it captures rich semantic interactions between modalities before prediction. Beyond simple concatenation, advanced techniques compute tensor products of modality-specific representations to model higher-order interactions [Fukui et al., 2016, Zadeh et al., 2017], or apply gating and attention mechanisms [Hori et al., 2017, Kiela et al., 2018, Tsai et al., 2019]. However, feature-level fusion methods can be vulnerable to noisy or corrupted modalities, which may significantly degrade overall performance [Ma et al., 2021]. To mitigate this issue, our framework constructs the joint representation as a linear combination of modality-specific embeddings, complemented by a pseudo representation explicitly designed to capture high-order (i.e., synergistic) interactions. The use of linear fusion weights offers full interpretability, enabling dynamic modality selection: when a modality is unreliable, its contribution to the final prediction is naturally suppressed.

2.2 Interpretability in Multimodal Learning

The heterogeneity of multimodal data, combined with their complex interdependencies, makes it challenging to interpret the prediction process and disentangle the contribution of each modality to the final decision [Liang et al., 2024, Binte Rashid et al., 2024]. Several conventional explainable artificial intelligence (XAI) approaches can be straightforwardly extended to the multimodal setting [Rodis et al., 2024]. For example, DIME [Lyu et al., 2022] applies LIME [Ribeiro et al., 2016] separately to each unimodal contribution and their interactions, assuming that the multimodal model is formed as an aggregation of these components. In another study [Wang et al., 2021], image data and metadata are jointly used for skin lesion diagnosis, where Grad-CAM [Selvaraju et al., 2017] is employed to interpret the image features, while kernel SHAP [Lundberg and Lee, 2017] is applied to explain the contribution of metadata. Recently, Zhu et al. [2025] and Wang et al. [2023] apply the information bottleneck (IB) principle [Tishby et al., 2000] to cross-modal feature attribution, improving interpretability in vision-language models [Radford et al., 2021] by filtering task-irrelevant information. However, these methods are fundamentally limited by their reliance on post-hoc explanations, applied only after model training. This creates a risk of inconsistency between the explanations and the model’s actual decision-making process, raising concerns about their faithfulness [Das and Rad, 2020].

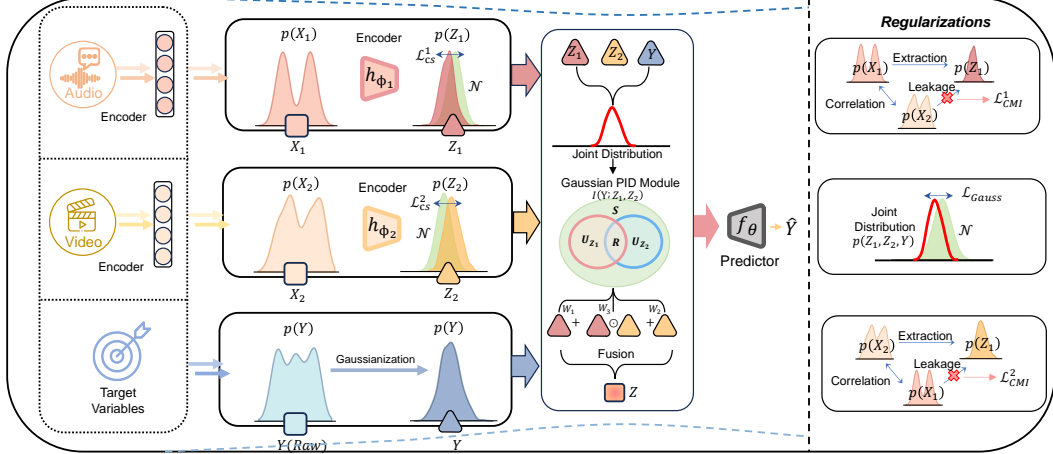


Figure 1: Framework of Partial Information Decomposition for Multimodal Regression (PIDReg), illustrated with video and audio modalities, where $P(X_1)$, $P(X_2)$, and $P(Y)$ denote empirical data distributions that may deviate from Gaussianity (e.g., skewed or heavy-tailed).

In contrast to existing methods that primarily offer *instance-level* interpretability in a *post-hoc* fashion, our approach emphasizes *intrinsic* interpretability by embedding explanatory mechanisms directly into the model design. This enables more transparent decision logic and direct explanations. Specifically, our method focuses on *modality-level* interpretability, identifying which modalities or cross-modal interactions are most critical to the decision-making process.

3 PIDReg: Partial Information Decomposition for Multimodal Regression

3.1 Overall Framework

Our PIDReg framework shown in Fig. 1 comprises two stochastic, modality-specific encoders, h_{ϕ_1} and h_{ϕ_2} ; an interpretable PID-guided feature fusion module; and a predictor f_θ operating on the fused features. Additional regularizers, including uniqueness information regularization and joint Gaussian regularization, are applied to ensure a rigorous implementation.

Given two modality-specific embeddings $R_1 = h_{\phi_1}(X_1)$, $R_2 = h_{\phi_2}(X_2)$ in \mathbb{R}^d , we introduce an adaptive linear–noise information bottleneck (IB) [Schulz et al., 2020] to regulate the information flow in each modality and enhance generalization. For each modality $m \in \{1, 2\}$, we compute empirical batch statistics mean vector μ_{R_m} and covariance matrix Σ_{R_m} and sample Gaussian noise $\epsilon_m \sim \mathcal{N}(\mu_{R_m}, \Sigma_{R_m})$ matched to R_m . The bottleneck output is then defined by a convex interpolation:

$$Z_m = \lambda_m R_m + (1 - \lambda_m) \epsilon_m, \quad (1)$$

where $\lambda_m \in (0, 1)$ is a trainable scalar. When $\lambda_m \approx 1$, R_m is preserved; when $\lambda_m \approx 0$, it is replaced by homoscedastic noise with identical first and second moments, effectively pushing $I(Z_m; X_m)$ toward zero. This formulation eliminates the need for reparameterization [Kingma et al., 2014] and enables an end-to-end learning of bottleneck strength while maintaining input variance for stable training. Further analysis on the effectiveness of this IB regularization, together with an ablation study, is provided in Appendix D.3.

After extracting modality-specific embeddings Z_1 and Z_2 , we aim to construct a fused representation Z as a linear combination of Z_1 , Z_2 , and \tilde{Z} :

$$Z = w_1 Z_1 + w_2 Z_2 + w_3 \tilde{Z}, \quad \text{s.t. } \tilde{Z} = Z_1 \odot Z_2, \quad (2)$$

where \tilde{Z} captures the *synergistic* effect that emerges only from the joint interaction between the two modalities. We expect the weights w_1 , w_2 , and w_3 to accurately reflect the contributions of Z_1 , Z_2 , and \tilde{Z} , respectively, thereby enhancing interpretability. The estimation of these weights is detailed in Section 3.1.1. The fused representation Z is passed through a predictor f_θ to generate final output.

In this work, we model the synergistic effect using the Hadamard (i.e., element-wise) product, defined as $\tilde{Z} = Z_1 \odot Z_2$. When synergy arises from feature-specific dependencies, and Z_1 and Z_2 are regularized to encode primarily unique

information (see Section 3.1.3), their element-wise product highlights cross-dimensional couplings between these unique components, which aligns with the concept of synergy. In practice, the Hadamard product is widely used to model interactions between two drug representations for drug synergy prediction [Al-Rabeah and Lakizadeh, 2022, Yang et al., 2023]. It has also been employed to fuse image and text representations in visual question answering [Fukui et al., 2016, Kim et al., 2016] and multimodal sentiment analysis [Zadeh et al., 2017].

3.1.1 Explainable Feature Fusion with Gaussian PID

Given two random variables Z_1 and Z_2 , and a target variable Y with joint distribution $P_{Z_1 Z_2 Y}$, the total information that (Z_1, Z_2) provides about Y is quantified by the mutual information $I(Y; Z_1, Z_2)$. The PID framework further decomposes this quantity into four non-negative components [Williams and Beer, 2010]:

$$\begin{cases} I(Y; Z_1, Z_2) = U_{Z_1} + U_{Z_2} + R + S \\ I(Y; Z_1) = U_{Z_1} + R \\ I(Y; Z_2) = U_{Z_2} + R, \end{cases} \quad (3)$$

where U_{Z_1} and U_{Z_2} denote the information *uniquely* provided by Z_1 and Z_2 , respectively. The term S captures the *synergistic* information that arises only through the joint interaction of Z_1 and Z_2 , and cannot be obtained from either alone. The term R represents the *redundant* information that is available in both Z_1 and Z_2 and can be extracted from either. Note that the redundancy in PID should not be confused with redundancy in decision-making contexts. Instead, it means that the same informative content about Y is accessible through either Z_1 or Z_2 , so once one source provides it, the other does not need to do so.

Although Eq. (3) provides a framework for interpretability through information decomposition, it defines four components with only three equations, resulting in an underdetermined system that admits infinitely many non-negative solutions. To resolve this ambiguity, one of the partial information components must be formally specified. In this work, we adopt the concept of union information $I^{\cup}(Y : Z_1; Z_2) := U_{Z_1} + U_{Z_2} + R$ [Bertschinger et al., 2014], which introduces an additional equation constraining the sum of unique information and redundancy through a constrained optimization problem. This additional constraint renders the system fully determined and enables a unique decomposition.

Definition 1 (Union Information [Bertschinger et al., 2014]). *The union information about Y present in both Z_1 and Z_2 is given by:*

$$\widetilde{I}^{\cup}(Y : Z_1; Z_2) := \min_{Q \in \Delta_P} I_Q(Y; Z_1, Z_2), \quad (4)$$

where $\Delta_P := \{Q_{YZ_1 Z_2} : Q_{YZ_1} = P_{YZ_1}, Q_{YZ_2} = P_{YZ_2}\}$, and I_Q is the mutual information under the joint distribution $Q_{YZ_1 Z_2}$. The remaining PID terms follow Eq. (3).

However, optimizing Eq. (4) for high-dimensional variables is computationally infeasible. To simplify the problem, we restrict the search space of Δ_P in Eq. (4) and assume that the joint distribution $P_{Z_1 Z_2 Y} \sim \mathcal{N}(\mu, \Sigma^P)$ is multivariate Gaussian, which enables closed-form expressions for mutual information terms in Eq. (3). For instance, $I(Y; Z_1, Z_2) = \frac{1}{2} \log \left(\frac{\det(\Sigma_{Z_1 Z_2})}{\det(\Sigma_{Z_1 Z_2 | Y})} \right)$. Note that this Gaussian assumption is not imposed on the original input data X_1, X_2 , or Y , but rather on the latent representations. Consequently, PIDReg fully accommodates real-world phenomena such as heavy tails, skewness, and even highly multimodal distributions, as demonstrated in our experiments. Further clarification of the Gaussian assumption rationale is provided in the Appendix A.1. This Gaussian assumption greatly simplifies the optimization and allows the problem in Eq. (4) to be reformulated as [Venkatesh et al., 2023]:

$$\widetilde{I}_G^{\cup}(Y : Z_1; Z_2) := \min_{\Sigma_{Z_1 Z_2 | Y}^Q} \frac{1}{2} \log \det \left(I + \sigma_Y^{-2} \begin{bmatrix} \Sigma_{Y Z_1}^P \\ \Sigma_{Y Z_2}^P \end{bmatrix}^T \left(\Sigma_{Z_1 Z_2 | Y}^Q \right)^{-1} \begin{bmatrix} \Sigma_{Y Z_1}^P \\ \Sigma_{Y Z_2}^P \end{bmatrix} \right) \quad \text{s.t.} \quad \Sigma_{Z_1 Z_2 | Y}^Q \succeq 0, \quad (5)$$

which is amenable to projected gradient descent [Riedmiller and Braun, 1993] and admits an analytical gradient. We refer interested readers to [Venkatesh et al., 2023] for more details.

After solving Eqs. (3) and (5), the fusion weights in Eq. (2) are computed based on the PID components. Since the redundancy R can be attributed to either modality-specific representation, we introduce a binary variable $\xi \sim \text{Bernoulli}(0.5)$ during training to stochastically control the assignment. The weights are computed as:

$$w_1 = \frac{U_{Z_1} + \xi R}{T}, \quad w_2 = \frac{U_{Z_2} + (1 - \xi)R}{T}, \quad w_3 = \frac{S}{T}, \quad \text{where } T = U_{Z_1} + U_{Z_2} + S + R. \quad (6)$$

This stochastic formulation ensures symmetric sharing of redundancy, reduces bias toward either modality. Note that, the above mechanism can be naturally extended to more than two modalities, as further discussed in the Appendix F.

3.1.2 Gaussian Regularization of the Joint Distribution $P_{Z_1 Z_2 Y}$

To encourage the marginal distribution $p(Z_m)$ to resemble a Gaussian, we adopt the CS divergence [Jenssen et al., 2006, Yu et al., 2025], which has recently gained renewed attention in representation learning [Tran et al., 2022, Yu et al., 2024a]. It is defined as:

$$D_{\text{CS}}(p(z); q(z)) = \log \left(\int q(z)^2 dz \right) + \log \left(\int p(z)^2 dz \right) - 2 \log \left(\int p(z)q(z) dz \right). \quad (7)$$

The motivation for using CS divergence, rather than the popular Kullback-Leibler (KL) divergence and maximum mean discrepancy (MMD) [Gretton et al., 2012], is discussed in the Appendix A.2.

In our setting, $p(z)$ denotes the probability density function of Z_m , $q(z) \sim \mathcal{N}(0, I)$ represents an isotropic Gaussian. Empirically, given M samples $\{z_i^p\}_{i=1}^M$ drawn from $p(z_m)$ and N samples $\{z_j^q\}_{j=1}^N$ drawn from $\mathcal{N}(0, I)$, the CS divergence $D_{\text{CS}}(p(z); \mathcal{N}(0, I))$ can be estimated as [Jenssen et al., 2006]:

$$\hat{D}_{\text{CS}}(p(z); \mathcal{N}(0, I)) = \log \left(\frac{\sum_{i,j=1}^M \kappa(z_i^p, z_j^q)}{M^2} \right) + \log \left(\frac{\sum_{i,j=1}^N \kappa(z_i^q, z_j^q)}{N^2} \right) - 2 \log \left(\frac{\sum_{i=1}^M \sum_{j=1}^N \kappa(z_i^p, z_j^q)}{MN} \right), \quad (8)$$

where κ is a kernel function with width σ such as Gaussian $\kappa(z_i, z_j) = \exp\left(-\frac{\|z_i - z_j\|^2}{2\sigma^2}\right)$. Owing to the symmetry of the CS divergence, the regularization on $p(Z_1)$ and $p(Z_2)$ is formulated as:

$$\mathcal{L}_{\text{CS}} = \hat{D}_{\text{CS}}(p(z_1); \mathcal{N}(0, I)) + \hat{D}_{\text{CS}}(p(z_2); \mathcal{N}(0, I)). \quad (9)$$

Additionally, we apply a rank-based, outlier-aware inverse normal transformation [Conover, 1999] to the target variable Y to approximate a normal distribution. However, regularizing the marginal distributions P_{Z_m} and P_Y does not ensure that the joint distribution $P_{Z_1 Z_2 Y}$ of Z_1 , Z_2 , and Y is multivariate Gaussian. To address this, we further introduce a regularization term $\mathcal{L}_{\text{Gauss}}$ to promote joint normality. Following Palmer et al. [2018], we apply whitening and vectorization to convert the multivariate Gaussianity test into a univariate Shapiro-Wilk (SW) test [Shapiro and Wilk, 1965].

We construct a feature matrix $F = \{f_i\}_{i=1}^n$ with $f_i = [Y_i, Z_{1,i}, Z_{2,i}]^\top \in \mathbb{R}^{2d+1}$, compute its sample mean \bar{f} and covariance matrix S , and apply the whitening transformation:

$$f_i^w = S^{-\frac{1}{2}}(f_i - \bar{f}). \quad (10)$$

Under the Gaussian assumption, the whitened samples f_i^w should follow $f_i^w \sim \mathcal{N}_{2d+1}(0, I)$.

We then vectorize the whitened matrix $F^w = [f_1^w, \dots, f_n^w]^\top \in \mathbb{R}^{n \times (2d+1)}$ as:

$$f_{\text{vec}} = \text{vec}(F^w) = \left(f_{11}^w, f_{12}^w, \dots, f_{1(2d+1)}^w, f_{21}^w, \dots, f_{n(2d+1)}^w \right)^\top \in \mathbb{R}^{n(2d+1) \times 1}. \quad (11)$$

The final SW test statistic is given by:

$$W = \left(\sum_{i=1}^{n(2d+1)} a_i f_{(i)}^w \right)^2 / \sum_{i=1}^{n(2d+1)} (f_i^w - \bar{f}^w)^2 \quad (12)$$

where $f_{(i)}^w$ is the i -th order statistic and a_i are coefficients under the standard normal distribution. If $W < W_\alpha(n(2d+1))$ at significance level α , the null hypothesis H_0 (normality) is rejected.

The regularization term is defined as:

$$\mathcal{L}_{\text{Gauss}} = -\log(W), \quad (13)$$

which approaches zero as $W \rightarrow 1$ (ideal Gaussianity), and increases otherwise.

3.1.3 Regularizing for Unique Information Extraction

To ensure that Z_1 and Z_2 primarily capture unique information from their respective modalities, we introduce an additional regularization term that explicitly minimizes the conditional mutual information (CMI) $I(Z_1; X_2|X_1)$ and $I(Z_2; X_1|X_2)$. For example, minimizing $I(Z_1; X_2|X_1)$ reduces the information that Z_1 retains about X_2 beyond what is already explained by X_1 . This encourages Z_1 to encode only information specific to X_1 that is independent of X_2 .

From a probabilistic perspective, the conditional independence between Z_1 and X_2 given X_1 implies that $p(Z_1|X_1, X_2) = p(Z_1|X_1)$. By the definition of conditional probability, this can be reformulated as the identity $p(X_1, X_2, Z_1)p(X_1) = p(X_1, X_2)p(X_1, Z_1)$. This observation again motivates the use of the CS divergence in Eq. (7) to measure the closeness between these two joint distributions as a proxy for conditional independence:

$$I_{\text{CS}}(Z_1; X_2|X_1) = D_{\text{CS}}(p(X_1, X_2, Z_1)p(X_1); p(X_1, X_2)p(X_1, Z_1)). \quad (14)$$

Importantly, this approach enables a closed-form estimation of CMI, as demonstrated in Proposition 1.

Proposition 1. *Given N observations $\{\mathbf{x}_{1,i}, \mathbf{x}_{2,i}, \mathbf{z}_{1,i}\}_{i=1}^N$ drawing from an unknown and fixed joint distribution $p(X_1, X_2, Z_1)$ in which $\mathbf{x}_{1,i} \in \mathbb{R}^{d_1}$, $\mathbf{x}_{2,i} \in \mathbb{R}^{d_2}$, and $\mathbf{z}_{1,i} \in \mathbb{R}^d$. Let $M \in \mathbb{R}^{N \times N}$ be the Gram (a.k.a., kernel) matrix for variable X_1 , that is, $M_{ji} = \exp\left(-\frac{\|\mathbf{x}_{1,j} - \mathbf{x}_{1,i}\|_2^2}{2\sigma^2}\right)$, in which σ is the kernel width. Likewise, let $K \in \mathbb{R}^{N \times N}$ and $L \in \mathbb{R}^{N \times N}$ be the Gram matrices for variables X_2 and Z_1 , respectively. The empirical estimator of Eq. (14) is given by:*

$$\begin{aligned} \widehat{I}_{\text{CS}}(Z_1; X_2|X_1) &= -2 \log \left(\sum_{j=1}^N \left(\left(\sum_{i=1}^N M_{ji} \right) \left(\sum_{i=1}^N K_{ji} M_{ji} \right) \left(\sum_{i=1}^N L_{ji} M_{ji} \right) \right) \right) + \\ &\quad \log \left(\sum_{j=1}^N \left(\left(\sum_{i=1}^N K_{ji} L_{ji} M_{ji} \right) \left(\sum_{i=1}^N L_{ji} \right)^2 \right) \right) + \log \left(\sum_{j=1}^N \left(\frac{\left(\sum_{i=1}^N K_{ji} L_{ji} \right)^2 \left(\sum_{i=1}^N L_{ji} M_{ji} \right)^2}{\left(\sum_{i=1}^N K_{ji} L_{ji} M_{ji} \right)} \right) \right). \end{aligned} \quad (15)$$

Estimator to $I(Z_2; X_1|X_2)$ can be derived similarly. Our final regularization is expressed as:

$$\mathcal{L}_{\text{CMI}} = \widehat{I}(Z_1; X_2|X_1) + \widehat{I}(Z_2; X_1|X_2). \quad (16)$$

3.2 Optimization and Algorithm

The overall loss function of our PIDReg framework is expressed as follows:

$$\mathcal{L} = \mathcal{L}_{\text{pred}} + \lambda_1 \mathcal{L}_{\text{CS}} + \lambda_2 \mathcal{L}_{\text{CMI}} + \lambda_3 \mathcal{L}_{\text{Gauss}}, \quad (17)$$

where λ_1 , λ_2 , and λ_3 are regularization weights. Here, $\mathcal{L}_{\text{pred}}$ denotes the mean squared error (MSE) between the ground-truth y and the prediction \hat{y} , while \mathcal{L}_{CS} , \mathcal{L}_{CMI} , and $\mathcal{L}_{\text{Gauss}}$ are defined earlier.

Formally, the optimization problem can be expressed as:

$$\min_{\theta, \varphi_1, \varphi_2, \mathbf{w}} \mathcal{L}(f_\theta, h_{\varphi_1}, h_{\varphi_2}, \mathbf{w}), \quad (18)$$

where $\mathbf{w} = [w_1, w_2, w_3]^T$ denotes fusion parameters (see Eq. (6)).

We design a two-stage optimization strategy based on the observation that the fusion parameter \mathbf{w} typically converges faster than the network parameters. In Stage I, all parameters are updated in an end-to-end manner. Once \mathbf{w} stabilizes or exhibits temporal consistency, we move to Stage II, where we optimize the following objective:

$$\min_{\theta, \varphi_1, \varphi_2} \mathcal{L}(f_\theta, h_{\varphi_1}, h_{\varphi_2}, \mathbf{w}^*), \quad (19)$$

where \mathbf{w}^* denotes the optimal fusion weight obtained at the end of Stage I.

In Stage II, the predictor f_θ and modality-specific encoders h_{φ_m} are updated according to Eq. (20) and Eq. (21), respectively:

$$f_\theta^{(t+1)} = f_\theta^{(t)} - \eta_{\text{pred}} \nabla_{f_\theta} \mathcal{L}_{\text{pred}}, \quad (20)$$

and,

$$h_{\varphi_m}^{(t+1)} = h_{\varphi_m}^{(t)} - \eta_{\text{encoder}} \nabla_{h_{\varphi_m}} (\lambda_1 \mathcal{L}_{\text{CS}}^m + \lambda_2 \mathcal{L}_{\text{CMI}}^m + \lambda_3 \mathcal{L}_{\text{Gauss}}). \quad (21)$$

We refer interested readers to Appendix C for a detailed description of the full algorithm, and to Appendix D.1 for an ablation study of the regularization components.

4 Experiments

4.1 Experiments on Synthetic Data

We first demonstrate the properties of our model on synthetic data, where the trade-offs between redundancy, synergy, and unique information are controllable. First, latent variables representing redundancy and unique information are

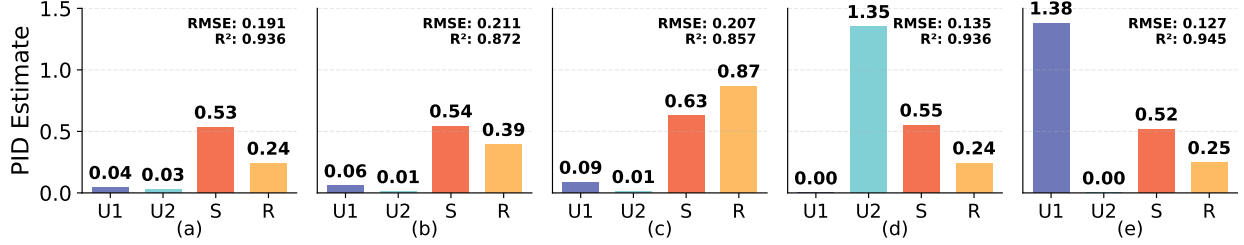


Figure 2: Estimated PID values when (a) $w_{u1} = 0$, $w_{u2} = 0$, $w_s = 0.75$, $w_r = 0.25$; (b) $w_{u1} = 0$, $w_{u2} = 0$, $w_s = 0.50$, $w_r = 0.50$; (c) $w_{u1} = 0$, $w_{u2} = 0$, $w_s = 0.25$, $w_r = 0.75$; (d) $w_{u1} = 0$, $w_{u2} = 0.80$, $w_s = 0.10$, $w_r = 0.10$; (e) $w_{u1} = 0.80$, $w_{u2} = 0$, $w_s = 0.10$, $w_r = 0.10$.

independently sampled from a standard normal distribution: $R, U_1, U_2 \sim \mathcal{N}(0, 1)$. The latent pair $[R, U_1]$ is then nonlinearly projected into a higher-dimensional observation space via a multi-layer perceptron (MLP):

$$X_1 = \tanh \left([R, U_1] W^{(1)} + b^{(1)} \right) W^{(2)} + b^{(2)} + \varepsilon_1, \quad \varepsilon_1 \sim \mathcal{N}(0, \sigma_1^2 I_{d_1}), \quad (22)$$

where the weights and biases are defined as $W^{(1)} \in \mathbb{R}^{2 \times h_1}$, $b^{(1)} \in \mathbb{R}^{h_1}$, $W^{(2)} \in \mathbb{R}^{h_1 \times d_1}$, and $b^{(2)} \in \mathbb{R}^{d_1}$, with all parameters initialized from $\mathcal{N}(0, \alpha^2)$. The second modality X_2 is generated analogously by applying an independent MLP to the latent pair $[R, U_2]$, producing $X_2 \in \mathbb{R}^{d_2}$.

The target variable Y is then constructed from these informational components through:

$$Y = w_r \tanh(R) + w_{u1} \sin(U_1) + w_{u2} \sin(U_2) + w_s U_1 U_2 + \varepsilon, \quad \varepsilon \sim \mathcal{N}(0, \sigma_\varepsilon^2), \quad (23)$$

where the product $U_1 U_2$ synergistically influence Y . By adjusting the weights w_r, w_{u1}, w_{u2} , and w_s , the relative contributions of redundancy, uniqueness, and synergy can be explicitly controlled. Experimental results in Fig. 2 show that PIDReg accurately estimates the relative strengths of the underlying generative factors, as reflected by the positive correlation with the true weights (i.e., the monotonic trend of S/R with respect to w_s/w_r) and the near-zero value of U when $w_u \approx 0$. Please refer to Appendix G.4.3 for a significance test and a detailed description.

4.2 Real-World Multimodal Regression

To rigorously evaluate the effectiveness and interpretability of the proposed PIDReg framework, we conduct comprehensive experiments on six real-world datasets spanning diverse domains, including healthcare, physics, affective computing, and robotics, covering both univariate and multivariate prediction tasks. For empirical comparison, PIDReg is evaluated against state-of-the-art multimodal learning methods, including MIB [Mai et al., 2022], MoNIG [Ma et al., 2021], MEIB [Zhang et al., 2022], and DER [Amini et al., 2020]. For large-scale datasets, we additionally compare with CoMM [Dufumier et al., 2025], a recent method that incorporates PID into multimodal contrastive learning. The performance of different approaches is evaluated on the test set using Root Mean Square Error (RMSE) and Pearson Correlation Coefficient (Corr). Experimental details are provided in the Appendix E.

CT Slices [Graf and Cavallaro, 2011] is a medical imaging dataset that integrates two modalities derived from 53,500 CT slices across 74 patients: bone structure histograms (240 features) and air inclusion histograms (144 features). The regression target is the axial position along the cephalocaudal axis, ranging from 0 (cranial vertex) to 180 (plantar surface). The dataset is split into 70% training, 10% validation, and 20% test sets. As shown in Table 1, our PIDReg achieves the lowest RMSE and highest correlation.

Metric	MIB	MoNIG	MEIB	DER	PIDReg
RMSE ↓	1.801	1.490	1.258	0.847	0.626
Corr ↑	0.997	0.996	0.999	1.000	1.000

Metric	MIB	MoNIG	MEIB	DER	PIDReg
RMSE ↓	15.18	14.59	14.04	12.37	10.37
Corr ↑	0.907	0.913	0.917	0.936	0.952

Table 1: CT Slice (left) and Superconductivity (right) regression (best results are shown in **bold**; second-best results are underlined. The same convention applies in all subsequent tables).

Superconductivity [Hamidieh, 2018] is a superconductivity dataset from physics, containing 21,263 material samples, each represented by two modalities: an 81-dimensional vector of chemical properties and an 86-dimensional vector

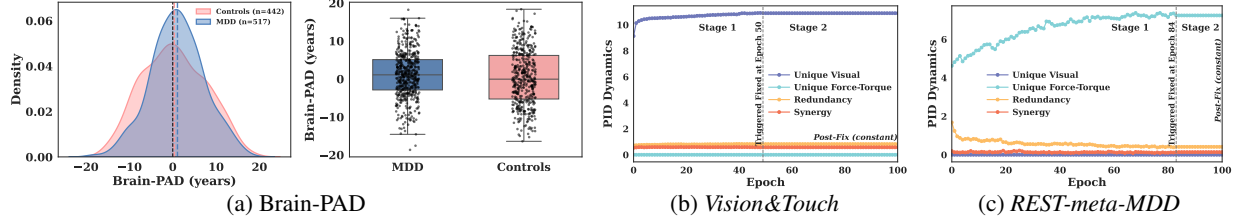


Figure 3: (a) Bias-corrected predicted age difference; (b, c) convergence curves of PID components.

derived from chemical formulas. The regression target is the superconducting critical temperature, a continuous variable ranging from 0 to 185. As shown in Table 1, our PIDReg achieves the lowest RMSE and highest correlation, further demonstrating its effectiveness.

CMU-MOSI [Zadeh et al., 2016] and **CMU-MOSEI** [Zadeh et al., 2018] contain 2,199 and 23,454 human-annotated sentiment labels, respectively, derived from short monologues and movie review video clips collected from YouTube. Both datasets provide three pre-extracted modalities: audio (A), text (T), and vision (V). The target variable is sentiment, represented as a continuous value in the range $[-3, 3]$. In each experiment, we select two modalities as input. Following the evaluation protocols in Pham et al. [2019], Liang et al. [2018], model performance is measured using 7-class accuracy (Acc7), binary accuracy (Acc2), F1-score, mean absolute error (MAE), and Corr. As shown in Table 2, our PIDReg consistently outperforms all baselines with Audio&Text and Visual&Text modalities, and achieves the second-best performance with the Audio&Visual modalities, where all competing methods exhibit a performance drop.

Method	CMU-MOSI					CMU-MOSEI				
	A ₇ ↑	A ₂ ↑	F1 ↑	MAE ↓	Corr ↑	A ₇ ↑	A ₂ ↑	F1 ↑	MAE ↓	Corr ↑
MIB [♡]	28.9	70.7	70.8	1.088	0.578	45.8	78.9	77.9	0.736	0.653
MoNIG [♡]	<u>31.9</u>	<u>79.1</u>	<u>79.1</u>	<u>0.976</u>	0.671	43.1	79.2	<u>79.0</u>	0.687	0.603
MEIB [♡]	23.9	60.6	60.5	1.246	0.415	40.3	62.4	64.0	0.789	0.414
DER [♡]	30.9	78.5	78.4	1.086	0.637	48.5	<u>79.9</u>	80.0	<u>0.637</u>	<u>0.655</u>
PIDReg [♡]	32.0	80.0	79.7	0.938	<u>0.662</u>	<u>47.4</u>	80.2	80.0	<u>0.634</u>	<u>0.662</u>
MIB [♣]	27.4	73.2	73.3	1.092	0.601	46.7	79.4	78.8	0.733	0.656
MonIG [♣]	29.9	78.1	78.0	1.046	0.627	44.2	80.2	80.2	0.680	0.606
MEIB [♣]	24.2	60.1	60.8	1.301	0.374	41.8	63.2	64.8	0.777	0.424
DER [♣]	<u>33.2</u>	<u>80.5</u>	<u>80.7</u>	<u>0.969</u>	0.666	46.6	<u>79.8</u>	80.2	<u>0.651</u>	<u>0.630</u>
PIDReg [♣]	37.2	80.8	80.9	0.947	<u>0.664</u>	47.0	80.6	80.2	<u>0.642</u>	<u>0.661</u>
MIB [◊]	14.4	47.7	40.7	1.511	0.146	41.4	62.2	63.2	1.004	0.149
MonIG [◊]	<u>15.9</u>	52.7	<u>55.6</u>	<u>1.428</u>	0.224	42.5	65.6	67.0	0.808	0.262
MEIB [◊]	15.2	45.0	52.2	1.478	0.152	<u>41.7</u>	53.9	58.1	<u>0.825</u>	0.178
DER [◊]	15.7	44.5	58.5	1.476	<u>0.212</u>	41.4	63.2	<u>65.6</u>	0.827	0.185
PIDReg [◊]	16.4	<u>52.3</u>	51.8	1.400	0.149	<u>41.7</u>	63.4	63.7	0.828	0.228

Table 2: Human sentiment analysis on CMU-MOSI and CMU-MOSEI (modality combinations are represented by symbols: \heartsuit (Audio-Text), \spadesuit (Visual-Text), and \diamondsuit (Audio-Visual)).

Metric	MIB	MonIG	MEIB	DER	CoMM	PIDReg	Metric	MIB	MonIG	MEIB	DER	CoMM	PIDReg
MSE \downarrow ($\times 10^{-4}$)	3.00	3408	6.19	498	1.34	<u>1.53</u>	MAE \downarrow	6.75	8.70	7.83	9.96	9.46	6.29
Corr \uparrow	<u>0.97</u>	0.82	0.96	0.85	0.98	<u>0.98</u>	Corr \uparrow	0.64	0.59	<u>0.65</u>	0.54	0.27	0.75

Table 3: Vision&Touch (left) and Brain-Age regression (right).

Vision&Touch [Lee et al., 2020] is a large-scale raw multimodal robotics dataset consisting of 150 trajectories of a triangular-peg-insertion task using a 7-DoF Franka Emika Panda robot. Each trajectory includes 1,000 synchronized time steps of visual, haptic, and proprioceptive signals. Following Liang et al. [2021], we formulate a regression task where selected proprioceptive dimensions at time $t + 1$ are predicted from other modalities at time t . Specifically, we use a four-dimensional subset (x, y, z , yaw) that represents the end-effector’s spatial position and yaw angle, thereby forming a *multivariate* prediction problem. To obtain modality-specific embeddings, we follow Dufumier et al. [2025]: visual inputs are processed using a ResNet-18 backbone pretrained on ImageNet, while force/torque sequences are encoded using a five-layer causal convolutional network [Bai et al., 2018] applied directly to the raw sensor readings. The results are shown in Table 3, evaluated via MSE and RV coefficient (Corr*) [Robert and Escoufier, 1976].

REST-meta-MDD [Yan et al., 2019] is the largest multimodal neuroimaging dataset for major depressive disorder (MDD), comprising 848 MDD patients and 794 healthy controls from 17 hospitals across China, along with metadata such as age and gender. We use T_1 -weighted sMRI and resting-state fMRI (rs-fMRI) as two input modalities to predict brain age. For 3D sMRI volumes, we use a 3D CNN encoder with channel and spatial attention. For rs-fMRI, we apply a Graph Isomorphism Network (GIN) [Xu et al., 2019] enhanced with graph attention and hierarchical pooling. We conduct nine groups of experiments, where in each group, data from 15 hospitals are randomly selected for training and the remaining 2 hospitals are used for testing, ensuring that each test site contains more than 100 samples to avoid biased evaluation. The results in Table 3 are averaged across all groups.

Fig. 3(a) shows the histogram of predicted age difference (PAD), defined as the deviation between the predicted and true chronological age, for patients and healthy controls, following standard linear bias correction [Smith et al., 2019]. PAD is commonly regarded as a robust biomarker for psychiatric diagnosis, as patients with conditions such as Alzheimer’s disease [Cole et al., 2017, Ly et al., 2020] and MDD [Han et al., 2021] often exhibit accelerated brain aging, resulting in a larger PAD. Our findings are consistent with existing medical evidence [Han et al., 2021, Luo et al., 2022]. The joint use of structural and functional brain connectivity offers a new way for brain age estimation.

4.3 Interpretability Analysis

Comp.	CT		SC		MOSI \heartsuit		MOSI \spadesuit		MOSI \diamond		MOSEI \heartsuit		MOSEI \spadesuit		MOSEI \diamond		V&T		MDD		
	Bone †	Air ‡	prop. †	form. ‡	A †	T ‡	V †	T ‡	A †	V ‡	A †	T ‡	V †	T ‡	A †	V ‡	Visual †	Touch ‡	fMRI †	sMRI ‡	
U_{Z_1}	0.045	0.375	0.103	0.053	0.023	0.021	0.023	0.012	10.90	0.000											
U_{Z_2}	0.067	0.001	0.209	0.058	0.152	0.025	0.030	0.042	0.000	7.240											
R	1.675	0.878	9.147	1.375	9.148	0.192	0.318	0.206	0.824	0.412											
S	1.147	0.394	0.312	4.228	0.331	0.298	0.690	0.290	0.575	0.140											

Table 4: Gaussian PID convergence values († and ‡ indicate X_1 and X_2 , respectively).

Figs. 3(b) and 3(c) depict the learning dynamics of each PID term over the entire training process for the V&T and MDD datasets. Table 4 summarizes the final converged values of the PID components. In **CT Slice** (CT), bone-density and air-content histograms encode nearly identical information about axial position, and thus redundancy dominates. In **Superconductivity** (SC), elemental physicochemical vectors provide the primary unique signal, while formula strings add little. This aligns with [Stanev et al., 2018], which highlights composition-aware features as key to T_c prediction.

In both **MOSI** and **MOSEI**, the presence of both high redundancy and high synergy across modality combinations suggests that sentiment analysis should not rely on a single modality alone. Moreover, Vision+Text is consistently dominated by synergy, as facial cues help disambiguate linguistic content. For example, [Castro et al., 2019] found that visual cues, such as neutral facial expressions or eye rolls, are critical for detecting sarcasm that cannot be captured by text alone. In contrast, Audio+Text typically exhibits notable redundancy. This aligns with the strong coupling between language and audio via word intonation [Zadeh et al., 2018]; e.g., prosody often reflects the emotional valence of lexical content.

In **Vision&Touch** (V&T), vision serves as the primary predictive engine, while tactile signals contribute little unique or synergistic information. This finding aligns with the visuo-tactile ablation study [Lee et al., 2019], suggesting that the visual modality alone may be sufficient to achieve reliable predictive performance. In **REST-meta-MDD** (MDD), sMRI is the dominant modality for brain age prediction, while rs-fMRI contributes minimally. This aligns with clinical evidence [Sun et al., 2024, Jónsson et al., 2019], which shows that sMRI is more informative than fMRI for brain age estimation. It is also consistent with [Cole et al., 2017, Liem et al., 2017], where morphometry alone achieves sub-5-year MAE and multimodal improvements are marginal. We refer interested readers to the Appendix D for additional ablation study results.

5 Conclusion

We propose PIDReg, a framework that seamlessly integrates PID into multimodal regression to improve both prediction accuracy and interpretability. PIDReg identifies the individual contributions of each modality and determines whether their interaction is dominated by redundancy or synergy. It is applicable to a wide range of data types, including vector data, 3D volume images, and graph-structured data, spanning diverse application domains. In particular, our results in brain age prediction align with current clinical evidence, highlighting the strong potential of PIDReg in biomedical science. PIDReg can be extended to three or more modalities, as detailed in the Appendix F. Limitations and future work are discussed in Appendix H.

References

- Luis R Soenksen, Yu Ma, Cynthia Zeng, Leonard Boussioux, Kimberly Villalobos Carballo, Liangyuan Na, Holly M Wiberg, Michael L Li, Ignacio Fuentes, and Dimitris Bertsimas. Integrated multimodal artificial intelligence framework for healthcare applications. *NPJ digital medicine*, 5(1):149, 2022.
- Mohammad Soleymani, David Garcia, Brendan Jou, Björn Schuller, Shih-Fu Chang, and Maja Pantic. A survey of multimodal sentiment analysis. *Image and Vision Computing*, 65:3–14, 2017.
- Chiori Hori, Takaaki Hori, Teng-Yok Lee, Ziming Zhang, Bret Harsham, John R Hershey, Tim K Marks, and Kazuhiko Sumi. Attention-based multimodal fusion for video description. In *Proceedings of the IEEE international conference on computer vision*, pages 4193–4202, 2017.
- Yao-Hung Hubert Tsai, Shaojie Bai, Paul Pu Liang, J Zico Kolter, Louis-Philippe Morency, and Ruslan Salakhutdinov. Multimodal transformer for unaligned multimodal language sequences. In *Proceedings of the conference. Association for computational linguistics. Meeting*, volume 2019, page 6558, 2019.
- Naftali Tishby, Fernando C Pereira, and William Bialek. The information bottleneck method. *arXiv preprint physics/0004057*, 2000.
- Sijie Mai, Ying Zeng, and Haifeng Hu. Multimodal information bottleneck: Learning minimal sufficient unimodal and multimodal representations. *IEEE Transactions on Multimedia*, 25:4121–4134, 2022.
- Arun Das and Paul Rad. Opportunities and challenges in explainable artificial intelligence (xai): A survey. *arXiv preprint arXiv:2006.11371*, 2020.
- Elena Tsankova, Eva Krumhuber, Andrew J Aubrey, Arvid Kappas, Guido Möllering, David Marshall, and Paul L Rosin. The multi-modal nature of trustworthiness perception. In *Proceedings of the international speech communication association (ISCA)*, pages 147–152. ISCA, 2015.
- Alexander Kraskov, Harald Stögbauer, and Peter Grassberger. Estimating mutual information. *Physical Review E—Statistical, Nonlinear, and Soft Matter Physics*, 69(6):066138, 2004.
- Artemy Kolchinsky. A novel approach to the partial information decomposition. *Entropy*, 24(3):403, 2022.
- Paul L Williams and Randall D Beer. Nonnegative decomposition of multivariate information. *arXiv preprint arXiv:1004.2515*, 2010.
- Paul Pu Liang, Yun Cheng, Xiang Fan, Chun Kai Ling, Suzanne Nie, Richard Chen, Zihao Deng, Nicholas Allen, Randy Auerbach, Faisal Mahmood, et al. Quantifying & modeling multimodal interactions: An information decomposition framework. *Advances in Neural Information Processing Systems*, 36:27351–27393, 2023.
- Jiayi Xin, Sukwon Yun, Jie Peng, Inyoung Choi, Jenna L Ballard, Tianlong Chen, and Qi Long. I2moe: Interpretable multimodal interaction-aware mixture-of-experts. In *Forty-second International Conference on Machine Learning*, 2025.
- William Jay Conover. *Practical nonparametric statistics*. john wiley & sons, 1999.
- Shujian Yu, Hongming Li, Sigurd Løkse, Robert Jenssen, and José C Príncipe. The conditional cauchy-schwarz divergence with applications to time-series data and sequential decision making. *IEEE Transactions on Pattern Analysis and Machine Intelligence*, 2025.
- Shujian Yu, Xi Yu, Sigurd Løkse, Robert Jenssen, and Jose C Príncipe. Cauchy-schwarz divergence information bottleneck for regression. In *The Twelfth International Conference on Learning Representations*, 2024a.
- Samuel Sanford Shapiro and Martin B Wilk. An analysis of variance test for normality (complete samples). *Biometrika*, 52(3-4):591–611, 1965.
- Songtao Li and Hao Tang. Multimodal alignment and fusion: A survey. *arXiv preprint arXiv:2411.17040*, 2024.
- Juan DS Ortega, Mohammed Senoussaoui, Eric Granger, Marco Pedersoli, Patrick Cardinal, and Alessandro L Koerich. Multimodal fusion with deep neural networks for audio-video emotion recognition. *arXiv preprint arXiv:1907.03196*, 2019.
- Amir Zadeh, Minghai Chen, Soujanya Poria, Erik Cambria, and Louis-Philippe Morency. Tensor fusion network for multimodal sentiment analysis. In *Proceedings of the 2017 Conference on Empirical Methods in Natural Language Processing*, pages 1103–1114, 2017.
- Shih-Cheng Huang, Anuj Pareek, Saeed Seyyedi, Imon Banerjee, and Matthew P Lungren. Fusion of medical imaging and electronic health records using deep learning: a systematic review and implementation guidelines. *NPJ digital medicine*, 3(1):136, 2020.
- Konstantin Hemker, Nikola Simidchievski, and Mateja Jamnik. HEALNet: Multimodal fusion for heterogeneous biomedical data. In *The Thirty-eighth Annual Conference on Neural Information Processing Systems*, 2024.

- Akira Fukui, Dong Huk Park, Daylen Yang, Anna Rohrbach, Trevor Darrell, and Marcus Rohrbach. Multimodal compact bilinear pooling for visual question answering and visual grounding. In *Conference on Empirical Methods in Natural Language Processing*, pages 457–468. ACL, 2016.
- Douwe Kiela, Edouard Grave, Armand Joulin, and Tomas Mikolov. Efficient large-scale multi-modal classification. In *Proceedings of the AAAI conference on artificial intelligence*, volume 32, 2018.
- Huan Ma, Zongbo Han, Changqing Zhang, Huazhu Fu, Joey Tianyi Zhou, and Qinghua Hu. Trustworthy multimodal regression with mixture of normal-inverse gamma distributions. *Advances in Neural Information Processing Systems*, 34:6881–6893, 2021.
- Paul Pu Liang, Amir Zadeh, and Louis-Philippe Morency. Foundations & trends in multimodal machine learning: Principles, challenges, and open questions. *ACM Computing Surveys*, 56(10):1–42, 2024.
- Maisha Binte Rashid, Md Shahidur Rahaman, and Pablo Rivas. Navigating the multimodal landscape: A review on integration of text and image data in machine learning architectures. *Machine Learning and Knowledge Extraction*, 6(3):1545–1563, 2024.
- Nikolaos Rodis, Christos Sardianos, Panagiotis Radoglou-Grammatikis, Panagiotis Sarigiannidis, Iraklis Varlamis, and Georgios Th Papadopoulos. Multimodal explainable artificial intelligence: A comprehensive review of methodological advances and future research directions. *IEEE Access*, 2024.
- Yiwei Lyu, Paul Pu Liang, Zihao Deng, Ruslan Salakhutdinov, and Louis-Philippe Morency. Dime: Fine-grained interpretations of multimodal models via disentangled local explanations. In *Proceedings of the 2022 AAAI/ACM Conference on AI, Ethics, and Society*, pages 455–467, 2022.
- Marco Tulio Ribeiro, Sameer Singh, and Carlos Guestrin. "why should i trust you?" explaining the predictions of any classifier. In *Proceedings of the 22nd ACM SIGKDD international conference on knowledge discovery and data mining*, pages 1135–1144, 2016.
- Sutong Wang, Yunqiang Yin, Dujuan Wang, Yanzhang Wang, and Yaochu Jin. Interpretability-based multimodal convolutional neural networks for skin lesion diagnosis. *IEEE transactions on cybernetics*, 52(12):12623–12637, 2021.
- Ramprasaath R Selvaraju, Michael Cogswell, Abhishek Das, Ramakrishna Vedantam, Devi Parikh, and Dhruv Batra. Grad-cam: Visual explanations from deep networks via gradient-based localization. In *Proceedings of the IEEE international conference on computer vision*, pages 618–626, 2017.
- Scott M Lundberg and Su-In Lee. A unified approach to interpreting model predictions. *Advances in neural information processing systems*, 30, 2017.
- Zhiyu Zhu, Zhibo Jin, Jiayu Zhang, NAN YANG, Jiahao Huang, Jianlong Zhou, and Fang Chen. Narrowing information bottleneck theory for multimodal image-text representations interpretability. In *The Thirteenth International Conference on Learning Representations*, 2025.
- Ying Wang, Tim GJ Rudner, and Andrew G Wilson. Visual explanations of image-text representations via multi-modal information bottleneck attribution. *Advances in Neural Information Processing Systems*, 36:16009–16027, 2023.
- Alec Radford, Jong Wook Kim, Chris Hallacy, Aditya Ramesh, Gabriel Goh, Sandhini Agarwal, Girish Sastry, Amanda Askell, Pamela Mishkin, Jack Clark, et al. Learning transferable visual models from natural language supervision. In *International conference on machine learning*, pages 8748–8763. PMLR, 2021.
- Karl Schulz, Leon Sixt, Federico Tombari, and Tim Landgraf. Restricting the flow: Information bottlenecks for attribution. In *International Conference on Learning Representations*, 2020.
- Diederik P Kingma, Max Welling, et al. Auto-encoding variational bayes. In *International conference on learning representations*, 2014.
- Mohammad Hussain Al-Rabeah and Amir Lakizadeh. Prediction of drug-drug interaction events using graph neural networks based feature extraction. *Scientific Reports*, 12(1):15590, 2022.
- Xinxing Yang, Jiachen Li, Xiao Kang, Guojin Pei, Keyu Liu, Genke Yang, and Jian Chu. Alnsynergy: a graph convolutional network with multi-representation alignment for drug synergy prediction. *arXiv preprint arXiv:2311.16207*, 2023.
- Jin-Hwa Kim, Sang-Woo Lee, Donghyun Kwak, Min-Oh Heo, Jeonghee Kim, Jung-Woo Ha, and Byoung-Tak Zhang. Multimodal residual learning for visual qa. *Advances in neural information processing systems*, 29, 2016.
- Nils Bertschinger, Johannes Rauh, Eckehard Olbrich, Jürgen Jost, and Nihat Ay. Quantifying unique information. *Entropy*, 16(4):2161–2183, 2014.

- Praveen Venkatesh, Corbett Bennett, Sam Gale, Tamina Ramirez, Greggory Heller, Severine Durand, Shawn Olsen, and Stefan Mihalas. Gaussian partial information decomposition: Bias correction and application to high-dimensional data. *Advances in Neural Information Processing Systems*, 36:74602–74635, 2023.
- Martin Riedmiller and Heinrich Braun. A direct adaptive method for faster backpropagation learning: The rprop algorithm. In *IEEE international conference on neural networks*, pages 586–591. IEEE, 1993.
- Robert Jenssen, Jose C Principe, Deniz Erdogmus, and Torbjørn Eltoft. The cauchy–schwarz divergence and parzen windowing: Connections to graph theory and mercer kernels. *Journal of the Franklin Institute*, 343(6):614–629, 2006.
- Linh Tran, Maja Pantic, and Marc Peter Deisenroth. Cauchy–schwarz regularized autoencoder. *Journal of Machine Learning Research*, 23(115):1–37, 2022.
- Arthur Gretton, Karsten M. Borgwardt, Malte J. Rasch, Bernhard Schölkopf, and Alexander Smola. A kernel two-sample test. *Journal of Machine Learning Research*, 13(25):723–773, 2012.
- Aaron Palmer, Dipak K Dey, and Jinbo Bi. Reforming generative autoencoders via goodness-of-fit hypothesis testing. In *UAI*, pages 1009–1019, 2018.
- Qi Zhang, Shujian Yu, Jingmin Xin, and Badong Chen. Multi-view information bottleneck without variational approximation. In *ICASSP 2022-2022 IEEE International Conference on Acoustics, Speech and Signal Processing (ICASSP)*, pages 4318–4322. IEEE, 2022.
- Alexander Amini, Wilko Schwarting, Ava Soleimany, and Daniela Rus. Deep evidential regression. *Advances in neural information processing systems*, 33:14927–14937, 2020.
- Benoit Dufumier, Javiera Castillo Navarro, Devis Tuia, and Jean-Philippe Thiran. What to align in multimodal contrastive learning? In *The Thirteenth International Conference on Learning Representations*, 2025.
- Kriegel H.-P. Schubert M. Poelsterl S. Graf, F. and A. Cavallaro. Relative location of CT slices on axial axis. UCI Machine Learning Repository, 2011. DOI: <https://doi.org/10.24432/C5CP6G>.
- Kam Hamidieh. A data-driven statistical model for predicting the critical temperature of a superconductor. *Computational Materials Science*, 154:346–354, 2018.
- Amir Zadeh, Rowan Zellers, Eli Pincus, and Louis-Philippe Morency. Multimodal sentiment intensity analysis in videos: Facial gestures and verbal messages. *IEEE Intelligent Systems*, 31(6):82–88, 2016.
- AmirAli Bagher Zadeh, Paul Pu Liang, Soujanya Poria, Erik Cambria, and Louis-Philippe Morency. Multimodal language analysis in the wild: Cmu-mosei dataset and interpretable dynamic fusion graph. In *Proceedings of the 56th Annual Meeting of the Association for Computational Linguistics (Volume 1: Long Papers)*, pages 2236–2246, 2018.
- Hai Pham, Paul Pu Liang, Thomas Manzini, Louis-Philippe Morency, and Barnabás Póczos. Found in translation: Learning robust joint representations by cyclic translations between modalities. In *Proceedings of the AAAI conference on artificial intelligence*, volume 33, pages 6892–6899, 2019.
- Paul Pu Liang, Ziyin Liu, AmirAli Bagher Zadeh, and Louis-Philippe Morency. Multimodal language analysis with recurrent multistage fusion. In *Proceedings of the 2018 Conference on Empirical Methods in Natural Language Processing*, pages 150–161, 2018.
- Michelle A Lee, Yuke Zhu, Peter Zachares, Matthew Tan, Krishnan Srinivasan, Silvio Savarese, Li Fei-Fei, Animesh Garg, and Jeannette Bohg. Making sense of vision and touch: Learning multimodal representations for contact-rich tasks. *IEEE Transactions on Robotics*, 36(3):582–596, 2020.
- Paul Pu Liang, Yiwei Lyu, Xiang Fan, Zetian Wu, Yun Cheng, Jason Wu, Leslie Chen, Peter Wu, Michelle A Lee, Yuke Zhu, et al. Multibench: Multiscale benchmarks for multimodal representation learning. *Advances in neural information processing systems*, 2021(DB1):1, 2021.
- Shaojie Bai, J Zico Kolter, and Vladlen Koltun. An empirical evaluation of generic convolutional and recurrent networks for sequence modeling. *arXiv preprint arXiv:1803.01271*, 2018.
- Paul Robert and Yves Escoufier. A unifying tool for linear multivariate statistical methods: the rv-coefficient. *Journal of the Royal Statistical Society Series C: Applied Statistics*, 25(3):257–265, 1976.
- Chao-Gan Yan, Xiao Chen, Le Li, Francisco Xavier Castellanos, Tong-Jian Bai, Qi-Jing Bo, Jun Cao, Guan-Mao Chen, Ning-Xuan Chen, Wei Chen, et al. Reduced default mode network functional connectivity in patients with recurrent major depressive disorder. *Proceedings of the National Academy of Sciences*, 116(18):9078–9083, 2019.
- Keyulu Xu, Weihua Hu, Jure Leskovec, and Stefanie Jegelka. How powerful are graph neural networks? In *International Conference on Learning Representations*, 2019.

- Stephen M Smith, Diego Vidaurre, Fidel Alfaro-Almagro, Thomas E Nichols, and Karla L Miller. Estimation of brain age delta from brain imaging. *Neuroimage*, 200:528–539, 2019.
- James H Cole, Rudra PK Poudel, Dimosthenis Tsagkrasoulis, Matthan WA Caan, Claire Steves, Tim D Spector, and Giovanni Montana. Predicting brain age with deep learning from raw imaging data results in a reliable and heritable biomarker. *NeuroImage*, 163:115–124, 2017.
- Maria Ly, Z Yu Gary, Helmet T Karim, Nishita R Muppidi, Akiko Mizuno, William E Klunk, Howard J Aizenstein, Alzheimer’s Disease Neuroimaging Initiative, et al. Improving brain age prediction models: incorporation of amyloid status in alzheimer’s disease. *Neurobiology of aging*, 87:44–48, 2020.
- Laura KM Han, Richard Dinga, Tim Hahn, Christopher RK Ching, Lisa T Eyler, Lyubomir Aftanas, Moji Aghajani, André Aleman, Bernhard T Baune, Klaus Berger, et al. Brain aging in major depressive disorder: results from the enigma major depressive disorder working group. *Molecular psychiatry*, 26(9):5124–5139, 2021.
- Yunsong Luo, Wenyu Chen, Jiang Qiu, and Tao Jia. Accelerated functional brain aging in major depressive disorder: evidence from a large scale fmri analysis of chinese participants. *Translational Psychiatry*, 12(1):397, 2022.
- Valentin Stanev, Corey Oses, A Gilad Kusne, Efrain Rodriguez, Johnpierre Paglione, Stefano Curtarolo, and Ichiro Takeuchi. Machine learning modeling of superconducting critical temperature. *npj Computational Materials*, 4(1):29, 2018.
- Santiago Castro, Devamanyu Hazarika, Verónica Pérez-Rosas, Roger Zimmermann, Rada Mihalcea, and Soujanya Poria. Towards multimodal sarcasm detection (an _obviously_ perfect paper). In *Proceedings of the 57th Annual Meeting of the Association for Computational Linguistics*, pages 4619–4629, 2019.
- Michelle A Lee, Yuke Zhu, Krishnan Srinivasan, Parth Shah, Silvio Savarese, Li Fei-Fei, Animesh Garg, and Jeannette Bohg. Making sense of vision and touch: Self-supervised learning of multimodal representations for contact-rich tasks. In *2019 International conference on robotics and automation (ICRA)*, pages 8943–8950. IEEE, 2019.
- Huili Sun, Saloni Mehta, Milana Khaitova, Bin Cheng, Xuejun Hao, Marisa Spann, and Dustin Scheinost. Brain age prediction and deviations from normative trajectories in the neonatal connectome. *Nature Communications*, 15(1):10251, 2024.
- Benedikt Atli Jónsson, Gyda Björnsdóttir, Thorgeir E Thorgeirsson, Lotta María Ellingsen, G Bragi Walters, Daniel Fanar Gudbjartsson, Hreinn Stefansson, Kari Stefansson, and Magnus Orn Ulfarsson. Brain age prediction using deep learning uncovers associated sequence variants. *Nature communications*, 10(1):5409, 2019.
- Franziskus Liem, Gaël Varoquaux, Jana Kynast, Frauke Beyer, Shahrzad Kharabian Masouleh, Julia M Huntenburg, Leonie Lampe, Mehdi Rahim, Alexandre Abraham, R Cameron Craddock, et al. Predicting brain-age from multimodal imaging data captures cognitive impairment. *Neuroimage*, 148:179–188, 2017.
- Diederik P Kingma, Max Welling, et al. An introduction to variational autoencoders. *Foundations and Trends® in Machine Learning*, 12(4):307–392, 2019.
- Shengjia Zhao, Jiaming Song, and Stefano Ermon. Infvae: Balancing learning and inference in variational autoencoders. In *Proceedings of the aaai conference on artificial intelligence*, volume 33, pages 5885–5892, 2019.
- Shujian Yu, Xi Yu, Sigurd Løkse, Robert Jenssen, and Jose C Principe. Cauchy-schwarz divergence information bottleneck for regression. In *12th International Conference on Learning Representations, ICLR 2024*, 2024b.
- Le Song, Jonathan Huang, Alex Smola, and Kenji Fukumizu. Hilbert space embeddings of conditional distributions with applications to dynamical systems. In *Proceedings of the 26th Annual International Conference on Machine Learning*, pages 961–968, 2009.
- Le Song, Kenji Fukumizu, and Arthur Gretton. Kernel embeddings of conditional distributions: A unified kernel framework for nonparametric inference in graphical models. *IEEE Signal Processing Magazine*, 30(4):98–111, 2013.
- Junhyung Park and Krikamol Muandet. A measure-theoretic approach to kernel conditional mean embeddings. *Advances in neural information processing systems*, 33:21247–21259, 2020.
- Yong Ren, Jun Zhu, Jialian Li, and Yucen Luo. Conditional generative moment-matching networks. *Advances in Neural Information Processing Systems*, 29, 2016.
- Andrew M Saxe, Yamini Bansal, Joel Dapello, Madhu Advani, Artemy Kolchinsky, Brendan D Tracey, and David D Cox. On the information bottleneck theory of deep learning. *Journal of Statistical Mechanics: Theory and Experiment*, 2019(12):124020, 2019.
- Kenji Kawaguchi, Zhun Deng, Xu Ji, and Jiaoyang Huang. How does information bottleneck help deep learning? In *International conference on machine learning*, pages 16049–16096. PMLR, 2023.

- Jeffrey Pennington, Richard Socher, and Christopher D Manning. Glove: Global vectors for word representation. In *Proceedings of the 2014 conference on empirical methods in natural language processing (EMNLP)*, pages 1532–1543, 2014.
- Gilles Degottex, John Kane, Thomas Drugman, Tuomo Raitio, and Stefan Scherer. Covarep—a collaborative voice analysis repository for speech technologies. In *2014 ieee international conference on acoustics, speech and signal processing (icassp)*, pages 960–964. IEEE, 2014.
- Kaiming He, Xiangyu Zhang, Shaoqing Ren, and Jian Sun. Deep residual learning for image recognition. In *Proceedings of the IEEE conference on computer vision and pattern recognition*, pages 770–778, 2016.
- Ed Bullmore and Olaf Sporns. Complex brain networks: graph theoretical analysis of structural and functional systems. *Nature reviews neuroscience*, 10(3):186–198, 2009.
- Sanghyun Woo, Jongchan Park, Joon-Young Lee, and In So Kweon. Cbam: Convolutional block attention module. In *Proceedings of the European conference on computer vision (ECCV)*, pages 3–19, 2018.
- Kaiming He, Xiangyu Zhang, Shaoqing Ren, and Jian Sun. Delving deep into rectifiers: Surpassing human-level performance on imagenet classification. In *Proceedings of the IEEE international conference on computer vision*, pages 1026–1034, 2015.
- Virgil Griffith and Christof Koch. Quantifying synergistic mutual information. In *Guided self-organization: inception*, pages 159–190. Springer, 2014.
- Jorge Nocedal and Stephen J Wright. *Numerical optimization*. Springer, 2006.
- Iman Beheshti, Scott Nugent, Olivier Potvin, and Simon Duchesne. Bias-adjustment in neuroimaging-based brain age frameworks: A robust scheme. *NeuroImage: Clinical*, 24:102063, 2019.

The appendix is organized into the following topics and sections:

Outline

- A** Design Motivation of PIDReg
 - A.1** Gaussian Assumption in Latent Space
 - A.2** The Motivation of CS Divergence
 - B** Proof of Proposition on Conditional Mutual Information Estimator
 - B.1** Definition
 - B.2** Estimator
 - C** Algorithm
 - D** Ablation Study
 - D.1** Regularization Component Ablation
 - D.2** Modality Ablation
 - D.3** Linear-Noise Information Bottleneck Ablation
 - E** Experimental Details
 - E.1** Raw Feature Encoder Architecture
 - E.2** Predictor Architecture
 - E.3** Training Strategies and Hyperparameter
 - F** Extension to Multivariate Gaussian and More than Two Modalities
 - F.1** Pragmatic Simplification for Three Modalities
 - F.2** Tractable Optimization Objective
 - F.3** Gradients and Optimization
 - F.4** Network Implementation
 - F.5** Experimental Results of Tri-Modal PIDReg
 - G** Extended Results
 - G.1** Computational Efficiency
 - G.2** Fine-Grained Results on Rest-meta-MDD
 - G.3** Large Scale Bimodal MNIST Regression Benchmark
 - G.4** Evaluation of PIDReg under Extreme Scenarios and Gaussian Distribution Shifts
 - H** Limitations and Future Work
-

A Design Motivations of PIDReg

A.1 Gaussian Assumption in the Latent Space

PIDReg does not impose any distributional assumptions on the original, complex input data X_1, X_2 , or Y , fully accommodating real world phenomena such as heavy-tailedness and skewness. Instead, the Gaussian assumption is imposed in the joint latent space formed by the transformed representations Z_1, Z_2 (obtained via the deep nonlinear encoders h_{ϕ_m}) together with the transformed target variable Y . Note that, this Y refers to the rank-based, outlier-aware inverse normal transformation of the target (rather than the raw Y), a procedure commonly adopted in neuroscience applications.

The role of the encoder h_{ϕ_m} is precisely to extract task-relevant, more structured, and compact information from raw inputs that may follow arbitrarily complex distributions. This design is conceptually aligned with modern generative models such as variational autoencoders (VAEs) [Kingma et al., 2019], which enforce a simple prior distribution (e.g., Gaussian) in the latent space to achieve regularization, disentanglement, and generative capability. In PIDReg, the Gaussian assumption serves as an inductive bias to guide the learning process, rather than as a rigid constraint.

We further introduce two differentiable regularization terms, designed based on the CS divergence, which actively guide the system toward Gaussianity. Notably, this active regularization mechanism is independent of any distributional assumption on the raw data itself.

In particular, our regularization based on the CS divergence is inspired by the well-known MMD-VAE [Zhao et al., 2019], where we replace the MMD with CS divergence to match the aggregated posterior $p(z)$ with a Gaussian prior $q(z)$. Compared to the traditional VAE regularization term $\mathbb{E}_{p(x)}[\text{KL}(p_\phi(z|x)\|q(z))]$, the CS-based (or MMD-based) penalty $\text{CS}(p_\phi(z), q(z))$ is operated on marginals and less restrictive, and notably helps mitigate the problem of uninformative latent codes, as discussed in Zhao et al. [2019].

A.2 The Motivation of CS Divergence

A central challenge in comparing probability distributions lies in selecting a divergence measure that is both theoretically sound and practically robust. Classical approaches such as the MMD and KL divergence represent two dominant paradigms: the integral probability metric (IPM) family and the f -divergence family, respectively. However, both exhibit critical limitations when applied to empirical distributions with limited support overlap or when robustly measuring distance between complex, high-dimensional densities.

A.2.1 CS Divergence against KL divergence: Stability and Symmetry

First, although both the KL divergence and the CS divergence can be employed to measure the difference or similarity between two entities (such as probability distributions or vectors), the CS divergence is considerably more stable than the KL divergence in that it relaxes the constraints on the supports of the distributions [Yu et al., 2024b]. For any two densities p and q , $D_{\text{KL}}(p; q)$ has finite values only if $\text{supp}(p) \subseteq \text{supp}(q)$ (otherwise, $p(x) \log \left(\frac{p(x)}{q(x)} \right) \rightarrow \infty$); whereas $D_{\text{KL}}(q; p)$ has finite values only if $\text{supp}(q) \subseteq \text{supp}(p)$. In contrast, $D_{\text{CS}}(p; q)$ is symmetric and always yields finite values unless the supports of p and q have no overlap, i.e., $\text{supp}(p) \cap \text{supp}(q) = \emptyset$ (see Fig. 4 for an illustration).

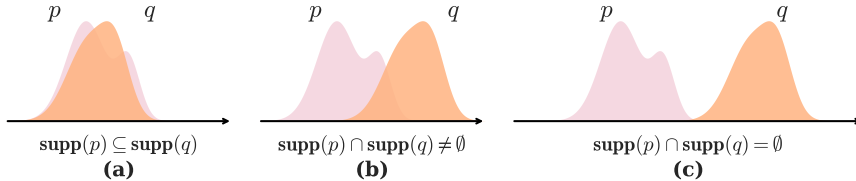


Figure 4: (a) $D_{\text{KL}}(p; q) \rightarrow \infty$, $D_{\text{KL}}(q; p) \rightarrow \infty$, $D_{\text{CS}}(p; q) \rightarrow \infty$; (b) $D_{\text{KL}}(p; q) \rightarrow \infty$, $D_{\text{KL}}(q; p) \rightarrow \infty$, $D_{\text{CS}}(p; q)$ finite; (c) $D_{\text{KL}}(p; q) \rightarrow \infty$, $D_{\text{KL}}(q; p) \rightarrow \infty$, $D_{\text{CS}}(p; q)$ finite.

Second, CS divergence is symmetric, eliminating the need to choose between $D_{\text{CS}}(p(z); \mathcal{N}(0, I))$ and $D_{\text{CS}}(\mathcal{N}(0, I); p(z))$.

A.2.2 CS Divergence against MMD: Efficiency in Estimator

MMD measures the difference in kernel mean embeddings:

$$\text{MMD}^2(P, Q) = \|\mu_P - \mu_Q\|_{\mathcal{H}}^2, \quad (24)$$

where μ_P and μ_Q are the kernel mean embeddings of distributions P and Q in the reproducing kernel Hilbert space \mathcal{H} .

By contrast, the empirical CS divergence estimator reduces to the cosine similarity between kernel-mean embeddings of two sample sets [Yu et al., 2024a]:

$$\hat{D}_{\text{CS}}(p; q) = -2 \log \left(\frac{\langle \mu_p, \mu_q \rangle_{\mathcal{H}}}{\|\mu_p\|_{\mathcal{H}} \|\mu_q\|_{\mathcal{H}}} \right) = -2 \log \cos(\mu_p, \mu_q). \quad (25)$$

While MMD admits closed-form estimators with clear physical interpretations when comparing marginal distributions P and Q , its extension to conditional distributions $p(Y|X)$ remains both theoretically unsettled and practically cumbersome: RKHS conditional-embedding (and related operator-based) approaches hinge on the conditional covariance operator:

$$C_{Y|X} = C_{YX} (C_{XX} + \lambda I)^{-1}, \quad (26)$$

which presupposes invertibility of the (uncentered) covariance C_{XX} and idealized stationarity—assumptions that routinely fail in high-dimensional or finite-sample regimes—and, more broadly, no universally accepted estimator for

conditional MMD has emerged, forcing costly kernel-matrix inversions or heavy regularization [Song et al., 2009, 2013, Park and Muandet, 2020, Ren et al., 2016].

In contrast, the CS divergence yields equally concise sample-based expressions for both marginal- and conditional-distributions comparison under far weaker hypotheses and with straightforward computation, motivating our choice to adopt CS divergence for simultaneous measurement of marginal and conditional distribution discrepancies.

B Proof of Proposition on Conditional Mutual Information Estimator

B.1 Definition

Consider an unknown but fixed joint distribution

$$p(X_1, X_2, Z_1), \quad (27)$$

from which we draw N observations $\{(x_{1i}, x_{2i}, z_{1i})\}_{i=1}^N$, where $x_{1i} \in \mathbb{R}^{d_1}$, $x_{2i} \in \mathbb{R}^{d_2}$, and $z_{1i} \in \mathbb{R}^d$. We are interested in the following CS divergence between two product distributions constructed from $p(X_1, X_2, Z_1)$:

$$D_{\text{CS}}(p(X_1, X_2, Z_1) p(X_1); p(X_1, X_2) p(X_1, Z_1)). \quad (28)$$

A more explicit expression of this divergence is:

$$\begin{aligned} & D_{\text{CS}}(p(X_1, X_2, Z_1) p(X_1); p(X_1, X_2) p(X_1, Z_1)) \\ &= -2 \log \left(\int p(X_1, X_2, Z_1) p(X_1) p(X_1, X_2) p(X_1, Z_1) \right) \\ &+ \log \left[\left(\int p^2(X_1, X_2, Z_1) p^2(X_1) \right) \left(\int p^2(X_1, X_2) p^2(X_1, Z_1) \right) \right]. \end{aligned} \quad (29)$$

In section B.2, we provide a kernel-based empirical estimator for Eq.(29).

B.2 Estimator

Approximation of the first integral. We start with the integral:

$$\int (p(X_1, X_2, Z_1) p(X_1); p(X_1, X_2) p(X_1, Z_1)), \quad (30)$$

which can be written as:

$$\mathbb{E}_{p(X_1, X_2, Z_1)} [p(X_1) p(X_1, X_2) p(X_1, Z_1)]. \quad (31)$$

Given the N i.i.d. samples $\{(x_{1i}, x_{2i}, z_{1i})\}_{i=1}^N$, a simple Monte Carlo approximation yields:

$$\frac{1}{N} \sum_{j=1}^N p(x_{1j}) p(x_{1j}, x_{2j}) p(x_{1j}, z_{1j}). \quad (32)$$

Next, we approximate each density term by a Gaussian kernel estimator. For instance,

$$p(x_{1j}, z_{1j}) \approx \frac{1}{N(\sqrt{2\pi}\sigma)^{d_1+d}} \sum_{i=1}^N \exp\left(-\frac{\|x_{1j} - x_{1i}\|^2}{2\sigma^2}\right) \exp\left(-\frac{\|z_{1j} - z_{1i}\|^2}{2\sigma^2}\right), \quad (33)$$

with analogous forms for $p(x_{2j}, z_{1j})$ and $p(z_{1j})$. Substituting these estimates into Eq.(32) and expanding the sums leads to a triple sum.

To simplify notation, define the following Gram (kernel) matrices:

- $M \in \mathbb{R}^{N \times N}$, the Gram matrix for X_1 , with

$$M_{ji} = \exp\left(-\frac{\|x_{1j} - x_{1i}\|^2}{2\sigma^2}\right).$$

- $K \in \mathbb{R}^{N \times N}$, the Gram matrix for X_2 , with

$$K_{ji} = \exp\left(-\frac{\|x_{2j} - x_{2i}\|^2}{2\sigma^2}\right).$$

- $L \in \mathbb{R}^{N \times N}$, the Gram matrix for Z_1 , with

$$L_{ji} = \exp\left(-\frac{\|z_{1j}-z_{1i}\|^2}{2\sigma^2}\right).$$

In these terms, the integral Eq.(30) can be approximated as (up to a constant factor involving N and σ):

$$\begin{aligned} & \int p(X_1, X_2, Z_1) p(X_1) p(X_1, X_2) p(X_1, Z_1) \\ & \approx \frac{1}{N^4 (\sqrt{2\pi} \sigma)^{d_1+d_2+3d}} \times \sum_{j=1}^N \left(\sum_{i=1}^N M_{ji} \right) \left(\sum_{i=1}^N K_{ji} M_{ji} \right) \left(\sum_{i=1}^N L_{ji} M_{ji} \right). \end{aligned} \quad (34)$$

Approximation of the remaining integrals. Similarly, we evaluate the two terms inside the large bracket of the CSn divergence:

- For $\int p^2(X_1, X_2, Z_1) p^2(Z_1)$ the same procedure yields:

$$\int p^2(X_1, X_2, Z_1) p^2(Z_1) \approx \frac{1}{N^4 (\sqrt{2\pi} \sigma)^{d_1+d_2+3d}} \sum_{j=1}^N \left(\sum_{i=1}^N K_{ji} L_{ji} M_{ji} \right) \left(\sum_{i=1}^N L_{ji} \right)^2. \quad (35)$$

- For $\int p^2(X_1, Z_1) p^2(X_2, Z_1)$ we obtain:

$$\int p^2(X_1, Z_1) p^2(X_2, Z_1) \approx \frac{1}{N^4 (\sqrt{2\pi} \sigma)^{d_1+d_2+3d}} \sum_{j=1}^N \left[\frac{\left(\sum_{i=1}^N K_{ji} L_{ji} \right)^2 \left(\sum_{i=1}^N L_{ji} M_{ji} \right)^2}{\sum_{i=1}^N K_{ji} L_{ji} M_{ji}} \right]. \quad (36)$$

Final Format. By combining these three approximations Eq.(34), Eq.(35) and Eq.(36), and omitting the common normalization factor, we obtain the following empirical estimator for Eq.(29):

$$\begin{aligned} \widehat{D}_{\text{CS}}(p(X_1, X_2, Z_1) p(X_1) ; p(X_1, X_2) p(X_1, Z_1)) = \\ -2 \log \left(\sum_{j=1}^N \left(\sum_{i=1}^N M_{ji} \right) \left(\sum_{i=1}^N K_{ji} M_{ji} \right) \left(\sum_{i=1}^N L_{ji} M_{ji} \right) \right) \\ + \log \left(\sum_{j=1}^N \left(\sum_{i=1}^N K_{ji} L_{ji} M_{ji} \right) \left(\sum_{i=1}^N L_{ji} \right)^2 \right) + \log \left(\sum_{j=1}^N \frac{\left(\sum_{i=1}^N K_{ji} L_{ji} \right)^2 \left(\sum_{i=1}^N L_{ji} M_{ji} \right)^2}{\sum_{i=1}^N K_{ji} L_{ji} M_{ji}} \right). \end{aligned} \quad (37)$$

□

C Algorithm

The pipeline of PIDReg is illustrated in Algorithm 1. In Stage 1, we initialize modality-specific encoders and employ a Gaussian PID-guided procedure to iteratively refine the weighting parameters, ensuring stable contributions from each modality. Once convergence is achieved, we fix these weights and move to Stage 2, where the network is fine-tuned under the current-static weighting scheme. Throughout the process, a parallel optimization step evaluates and updates the fused representation, ultimately yielding a robust, interpretable prediction.

Regarding the PID-converged check in Algorithm 1, it is defined as follows: let $G^t = \{U_{Z_1}^t, U_{Z_2}^t, R^t, S^t\}$ denote the average of the four parameters computed for each batch in the i -th iteration. Subsequently, we apply:

$$\delta^t = \|G^t - G^{t-1}\|_\infty < \epsilon, \quad (38)$$

when $\delta^t < \epsilon$ for K consecutive epochs, we establish $\mathbf{w}^* = \mathbf{w}^t$ as the optimal fusion weights. In practice, we set $K = 5$ and $\epsilon = 0.01$ to ensure stable convergence across stochastic minibatches while avoiding unnecessary training overhead.

Algorithm 1 PIDReg Algorithm

Require: Multimodal inputs $\{X_1, X_2\}$, target Y

Ensure: Prediction \hat{y} , information decomposition $\{U_{Z_1}, U_{Z_2}, R, S\}$

- 1: Initialize encoders h_{ϕ_m} , predictor f_θ , learnable IB parameters λ_m^b , fusion weights $\mathbf{w} = [w_1, w_2, w_3]$ and PID convergence flag $Converged \leftarrow false$
- 2: **while** not converged **do**
- 3: **for** each batch **do**
- 4: **for** $m \in \{1, 2\}$ **do**
- 5: $R_m = h_{\phi_m}(X_m)$ ▷ Raw Representations
- 6: $Z_m = \lambda_m^b \cdot R_m + (1 - \lambda_m^b) \cdot \mathcal{N}(\mu_{R_m}, \sigma_{R_m}^2)$ ▷ IB Mechanism
- 7: $\mathcal{L}_{CS} = \sum_{i=1}^2 \widehat{D}_{CS}(p(z_i); \mathcal{N}(0, I))$ ▷ Marginal Gaussianity
- 8: **end for**
- 9: $\mathcal{L}_{cmi} = \widehat{I}(Z_1; X_2 | X_1) + \widehat{I}(Z_2; X_1 | X_2)$ ▷ Unique Information Guarantee
- 10: **if** not PID-converged **then**
- 11: $\Sigma^P \leftarrow$ Estimate covariance matrix for (Z_1, Z_2, Y)
- 12: $\{U_{Z_1}, U_{Z_2}, R, S\} \leftarrow$ Gaussian PID decomposition of Σ^P
- 13: $\mathbf{w} \leftarrow [\frac{U_{Z_1}+R}{T}, \frac{U_{Z_2}}{T}, \frac{S}{T}]^T$ where $T = U_{Z_1} + U_{Z_2} + R + S$
- 14: $\mathcal{L}_{Gauss} =$ Gaussian normality deviation of (Z_1, Z_2, Y)
- 15: Check PID convergence criteria, update convergence flag if stable
- 16: **end if**
- 17: $Z = w_1 Z_1 + w_2 Z_2 + w_3 (Z_1 \odot Z_2)$ ▷ Information-weighted Fusion
- 18: $\hat{y} = f_\theta(Z)$ ▷ Prediction
- 19: $\mathcal{L}_{pred} = MSE(\hat{y}, y)$ ▷ Prediction Loss
- 20: Update network parameters and λ_m^b using respective optimizers
- 21: **end for**
- 22: Validate and adjust learning rates
- 23: **end while**
- 24: **return** Trained model with fixed optimal fusion weights \mathbf{w}^*

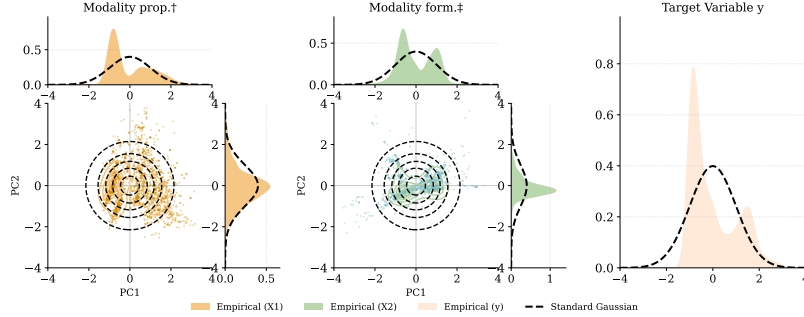
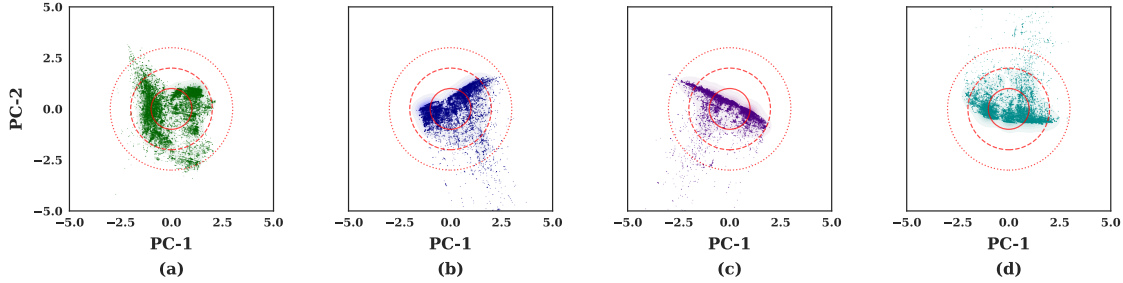
D Ablation Study**D.1 Regularization Component Ablation**

In our work, we introduce three regularization terms, \mathcal{L}_{CS} , \mathcal{L}_{Gauss} , and \mathcal{L}_{CMI} , which serve two distinct purposes. The \mathcal{L}_{CS} and \mathcal{L}_{Gauss} terms impose constraints on the marginal and joint distributions, respectively, to ensure that the resulting latent representation $P(Z_1, Z_2, Y)$, closely approximates a Gaussian distribution. In contrast, \mathcal{L}_{CMI} penalizes information leakage between Z_1 and X_2 as well as between Z_2 and X_1 , thereby guaranteeing that the feature fusion guided by the PID module's learned weights remains interpretable and faithful. In section D.1, we perform two ablations (section D.1.1, section D.1.2) to evaluate.

D.1.1 Joint Gaussian Guarantee

Taking the *Superconductivity* as an example, the empirical distributions of the raw inputs X_1 and X_2 are shown in Fig. 5, where one can observe severe skewness and non-Gaussianity. It is worth emphasizing that PIDReg does not rely on any distributional assumptions about the input data itself, rather, it aims to learn a Gaussian representation in the latent space. For visualization, the latent features of X_1 and X_2 are individually projected into two dimensions using Principal Component Analysis (PCA) with whitening, while the target variable Y , being one-dimensional, is directly shown without projection.

To further illustrate how PIDReg learns such a Gaussian system from highly non-Gaussian real world data, and to highlight the role of each Gaussianity regularizer, we ablated one or both Gaussianity regularizers (\mathcal{L}_{CS} , \mathcal{L}_{Gauss}), recorded the joint latent representations (Z_1, Z_2, Y) at the epoch when the PID module converged. To enable consistent visual comparison across different ablation settings and the full-loss baseline, we apply PCA with whitening on the joint representations to obtain two-dimensional projections. The resulting 2D distributions are overlaid with reference circles at 1σ , 2σ , and 3σ radii of a standard normal distribution. This enables an intuitive assessment of distributional concentration, isotropy, and deviation from Gaussianity, as illustrated in Fig. 6.

Figure 5: Distributions of $P(X_1)$, $P(X_2)$ and raw $P(Y)$.Figure 6: Visualization of the ablation study on joint latent distributions $P(Z_1, Z_2, Y)$ under different loss configurations: (a) full loss; (b) without the \mathcal{L}_{CS} term; (c) without the \mathcal{L}_{Gauss} term; (d) without both \mathcal{L}_{CS} and \mathcal{L}_{Gauss} terms. —, ·····, and -·— denote the 1 σ , 2 σ and 3 σ contours of a standard Gaussian distribution.

In Fig. 6(a), the full-loss embeddings cluster tightly at the origin. Removing \mathcal{L}_{CS} (b) shifts the cloud along PC-1 with heavy tails beyond 2 σ and 3 σ . Removing \mathcal{L}_{Gauss} (c) preserves centering but produces a diagonally elongated distribution. Omitting both (d) yields a highly anisotropic cloud with tails scattered well beyond 3 σ . \mathcal{L}_{CS} enforces mean zero and unit covariance, while \mathcal{L}_{Gauss} corrects skewness and kurtosis; dropping any component causes mean shifts, anisotropic scaling, and non-Gaussian distortions as the encoder focuses on prediction error.

D.1.2 Unique Information Extraction Guarantee

\mathcal{L}_{CMI} does not act directly on the joint distribution, it ensures that each modality’s latent encoding captures only the unique information of that modality, preventing irrelevant cross-modal redundancy from leaking into the other modality’s representation. If the \mathcal{L}_{CMI} is effective, then, in theory, Z_1 (resp. Z_2) should contain no or less information about X_2 (resp. X_1). Theoretically, consider the conditional mutual information $I(X_1; Z_2 | X_2)$. If $I(X_1; Z_2 | X_2) \approx 0$, then by the identity $I(X_1; Z_2 | X_2) = I(X_1; Z_2, X_2) - I(X_1; X_2)$, we obtain $I(X_1; Z_2, X_2) \approx I(X_1; X_2)$, i.e., the combined pair (Z_2, X_2) provides no additional information about X_1 beyond X_2 alone. Consequently, the mapping $(Z_2, X_2) \rightarrow X_1$ behaves almost identically to $X_2 \rightarrow X_1$.

Prediction	Full Loss		$-\mathcal{L}_{CMI}$	
	MSE \downarrow	$R^2\uparrow$	MSE \downarrow	$R^2\uparrow$
$X_2 \rightarrow X_1$	0.073	0.928	0.073	0.928
$Z_2 \rightarrow X_1$	0.670	0.334	0.155	0.846
$(Z_2, X_2) \rightarrow X_1$	0.089	0.911	0.089	0.912
$X_1 \rightarrow X_2$	0.619	0.380	0.619	0.380
$Z_1 \rightarrow X_2$	0.779	0.166	0.664	0.407
$(Z_1, X_1) \rightarrow X_2$	0.642	0.311	0.620	0.388

Table 5: Cross-prediction performance under Full Loss and without \mathcal{L}_{CMI} .

To verify this empirically, we record—for both the best-performing full-loss model and the model trained without \mathcal{L}_{CMI} —latent codes Z_1, Z_2 alongside their corresponding inputs X_1, X_2 , and apply the cross-prediction schemes listed

in Table 5. We then employ identical three-layer MLP probes (256 hidden units, LayerNorm, ReLU, dropout) for each of the six cross-modal regression tasks. The results align with our theoretical analysis: under full loss, $Z_2 \rightarrow X_1$ and $Z_1 \rightarrow X_2$ yield $R^2 \approx 0.34$ and 0.17 , respectively, indicating minimal information leakage; omitting \mathcal{L}_{CMI} causes R^2 to rise to 0.846 and 0.407 , demonstrating severe leakage. Moreover, joint regressors $(Z_2, X_2) \rightarrow X_1$ and $(Z_1, X_1) \rightarrow X_2$ confirm that any leaked information is redundant with each modality’s raw input.

The incorporation of \mathcal{L}_{CS} , $\mathcal{L}_{\text{Gauss}}$, and \mathcal{L}_{CMI} underpins the reliability of the PIDReg framework from both distributional alignment and information-theoretic interpretability perspectives, rendering each component indispensable.

D.2 Modality Ablation

As presented in the main paper’s Interpretability Analysis section, we quantify each modality’s contribution to prediction performance via PIDReg on multiple datasets. Notably, on the ***Vision&Touch*** dataset, Visual provides substantial unique information while Touch’s unique contribution is nearly zero; similarly, on ***Rest-meta-MDD***, sMRI yields significant unique content whereas fMRI does not. We thus hypothesize that (i) using only Visual on Vision&Touch will match the dual-modality baseline, but using only Touch will degrade performance markedly, and (ii) on Rest-meta-MDD, sMRI alone will suffice, whereas fMRI alone will fail. To test this, we conduct modal ablations by disabling the PID computation and fusion mechanism in PIDReg and instead assigning a fixed weight of 1 to the chosen modality, with all other components held constant.

Metric	Full	Visual-only	Touch-only	Metric	Full	sMRI-only	fMRI-only
MSE \downarrow ($\times 10^{-4}$)	1.53	1.84	93.5	MAE \downarrow	6.29	6.56	10.3
Corr \uparrow	0.98	0.98	0.05	Corr \uparrow	0.75	0.75	0.04

Table 6: Modality ablation experiments results: Vision&Touch (left) and Rest-meta-MDD (right).

The results in Table 6 fully validate our hypothesis, demonstrating that the PIDReg-derived information decomposition provides valuable guidance for both modality fusion and modality selection.

D.3 Linear-Noise Information Bottleneck Ablation

The linear noise injection in the information bottleneck framework, as formulated in Eq.(1), serves three fundamental purposes in our multimodal learning architecture:

- **Ensuring meaningful computation of information-theoretic terms.** The injection of noise effectively transforms a deterministic mapping $\bar{X} \rightarrow Z$ into a stochastic transformation. This stochasticity is essential for enabling meaningful and robust information-theoretic estimation, as purely deterministic mappings can exhibit pathological behavior, including infinite mutual information values under continuous variable settings, as previously established by Saxe et al. [2019].
- **Enhancing generalization capability.** The Information Bottleneck mechanism has been demonstrated, both empirically and theoretically [Kawaguchi et al., 2023], to discard irrelevant or noisy details in the input \bar{X} , thereby improving the model’s generalization performance.
- **Facilitating PID computation.** The injection of Gaussian noise into R_m shifts the marginal distribution of Z_m toward a Gaussian distribution, which is a prerequisite for our Gaussian PID component optimization framework.

Rather than manually selecting the noise parameter, λ_m is optimized through gradient-based learning. In our implementation, we introduce an unconstrained real-valued latent parameter λ'_m and define the bounded noise parameter as:

$$\lambda_m = \sigma(\lambda'_m) = \frac{1}{1 + e^{-\lambda'_m}}, \quad \lambda'_m \in \mathbb{R}, \quad \lambda_m \in (0, 1), \quad (39)$$

where σ denotes the sigmoid function. This reparameterization enables the utilization of unconstrained optimizers (e.g., Adam) to train the bounded variable λ_m indirectly. The gradient of λ'_m is computed with respect to the total loss $\mathcal{L}_{\text{total}}$, yielding the update rule:

$$\lambda'_{m,(t+1)} = \lambda'_{m,(t)} - \eta_\lambda \text{AdamUpdate} \left(\frac{\partial \mathcal{L}_{\text{total}}}{\partial \lambda'_{m,(t)}} \right), \quad (40)$$

where η_λ represents the learning rate for λ_m . Through this adaptive mechanism, the contributions of R_m and ϵ_m are dynamically balanced, enabling the information bottleneck to discover the optimal trade-off between preserving predictive information and satisfying regularization and interpretability constraints.

Table 7 presents the convergence values of λ_m across different datasets and modality configurations. The results demonstrate that noise injection consistently plays a significant role in MOSI and MOSEI datasets, particularly for the X_1 modality.

Comp.	CT		SC		MOSI $^\heartsuit$		MOSI $^\spadesuit$		MOSI $^\diamondsuit$		MOSEI $^\heartsuit$		MOSEI $^\spadesuit$		MOSEI $^\diamondsuit$		V&T		MDD	
	Bone †	Air ‡	prop. †	form. ‡	A †	T ‡	V †	T ‡	A †	V ‡	A †	T ‡	V †	T ‡	A †	V ‡	Visual †	Touch ‡	fMRI †	sMRI ‡
λ_1	0.99		0.99		0.69		0.98		0.99		0.85		0.77		0.80		0.99		0.99	0.98
λ_2	0.99		0.99		0.89		0.99		0.95		0.99		0.99		0.99		0.99		0.99	0.98

Table 7: λ convergence values († and ‡ indicate X_1 and X_2 , respectively).

To further substantiate the necessity of the information bottleneck component, we conducted an ablation study wherein λ_m was fixed to 1 for both CT Slice and Superconductivity datasets, with all other hyperparameters held constant. The comparative results are presented in Table 8.

Metric	CT	CT($\lambda_m = 1$)	SC	SC($\lambda_m = 1$)
RMSD \downarrow	0.626	0.843	10.37	10.44
Corr \uparrow	1.000	0.999	0.940	0.912

Table 8: Linear-noise information bottleneck ablation results.

These experimental findings confirm that even when λ_m is set to a relatively large value, the linear noise information bottleneck remains essential for enabling the critical deterministic-to-stochastic transition and maintaining the robustness of the PIDReg framework. The degradation in performance metrics when the information bottleneck is disabled ($\lambda_m = 1$) further substantiates the necessity of this component within our proposed methodology.

This empirical evidence reinforces the theoretical importance of the linear noise information bottleneck mechanism in achieving effective multimodal representation learning through information-theoretic regularization.

E Experimental Details

E.1 Raw Feature Encoder Architecture

All comparative experiments in this paper adopt a consistent encoder architecture to ensure fairness of comparison. The specific encoder used for each dataset is detailed as follows:

For both **CT Slice** and **Superconductivity**, each raw feature encoder is a symmetric three-stage MLP that successively compresses the original D -dimensional input into a d_m -dimensional embedding via $D \rightarrow HL \rightarrow \frac{HL}{2} \rightarrow d_m$, where HL is the hidden-layer dimensionality (a tunable hyperparameter controlling model capacity). Each linear projection is followed by BatchNorm1d, in-place ReLU, and dropout (with dropout rate $p = 0.3$ after the first layer and $p = 0.2$ after the second), and the final d_m -dimensional output is again normalized via BatchNorm1d to stabilize feature statistics. This uniform, modality-agnostic design yields compact embeddings, ensures robust gradient flow, and mitigates overfitting.

For both **CMU-MOSI**, **CMU-MOSEI**, following Pennington et al. [2014], Degottex et al. [2014], Ma et al. [2021], we employ an identical two-stage raw feature encoder that maps the input sequence $\mathbf{X} \in \mathbb{R}^{T \times d_{in}}$ for each modality (text, audio, vision) to a compact, context-aware embedding. First, a point-wise convolution projects each time step via

$$\mathbf{U} = \text{Dropout}(\text{LeakyReLU}(\text{BatchNorm1d}(\text{Conv1d}_{d_{in} \rightarrow d_m}(\mathbf{X}))). \quad (41)$$

Next, we transpose \mathbf{U} to shape (T, batch, d_m) , add fixed sinusoidal positional embeddings, and feed the sum into L stacked Transformer-encoder layers—each comprising H -head self-attention, residual connections, layer normalization, and a two-layer feed-forward network. Finally, the raw embedding is obtained by extracting the feature vector at the last time step, $\mathbf{h}_T \in \mathbb{R}^{d_m}$.

For **Vision&Touch**, we employ two modality-specific raw encoders that map the native sensor readings directly into feature vectors prior to information bottleneck mechanism: **Vision Encoder** uses a ResNet-18 pretrained on

ImageNet [He et al., 2016] (truncated before the final classification layer): Conv1 (7×7 kernel, stride 2, padding $3 \rightarrow 64$ channels; BatchNorm; ReLU), MaxPool (3×3 , stride 2), four residual stages (each with two basic blocks of conv $3 \times 3 \rightarrow$ BatchNorm \rightarrow ReLU and downsampling at the start of stages 2–4), a global average pool to yield a 512-dimensional vector, and a final linear projection ($512 \rightarrow d_1$) with BatchNorm1d. **Touch Encoder**: raw force trajectories $\mathbf{F} \in \mathbb{R}^{T \times 6}$ are processed by a sequence of 1D convolutions over time (kernel size 5), each with BatchNorm1d and ReLU, then collapsed via global max- or average-pooling, and finally mapped to d_2 dimensions by a linear layer [Lee et al., 2020, Dufumier et al., 2025].

For **Rest-meta-MDD**, fMRI is modeled as $G = (V, E)$ with Fisher- z edges. An optional E -dim node-ID embedding (per emb_style) is concatenated to features [Bullmore and Sporns, 2009]. We apply L GIN layers

$$x_v^{(l+1)} = \text{MLP}(x_v^{(l)} + \sum_{u \in \mathcal{N}(v)} x_u^{(l)}), \quad (42)$$

(hid. size H , out O , with dropout/BatchNorm), followed by two residual GATConv layers (4 heads, head-dim $O/4$), a node-wise MLP + sigmoid attention, and two SAGPooling stages (ratios 0.8, 0.6) each with global mean-pooling. Pooled vectors are summed and passed through Linear($O \rightarrow O$) – BN – ReLU – Dropout to yield the raw O -dim embedding. Normalized smRI volumes feed a six-stage 3D CNN: the first $L - 1$ blocks use either standard conv (3^3 , stride-2 pool, BN, ReLU) or depthwise-separable conv; the final block is a 1^3 conv. After each conv (except last) we optionally apply ChannelAttention (avg/max \rightarrow MLP \rightarrow sigmoid) and SpatialAttention (avg/max \rightarrow conv \rightarrow sigmoid) [Woo et al., 2018]. A final 3D avg-pool over $[5 \times 6 \times 5]$ produces a C -dim vector, then Linear($C \rightarrow C$)–BN–ReLU–Dropout yields the raw C -dim embedding.

E.2 Predictor Architecture

The regression head is a three-stage MLP that nonlinearly maps the fused latent embedding of dimension d to a scalar. The first stage applies Linear($d \rightarrow H$), followed by BatchNorm1d, in-place ReLU, and Dropout($p = 0.3$) to capture high-capacity feature interactions. The second stage performs Linear($H \rightarrow H/2$), plus BatchNorm1d, ReLU, and Dropout($p = 0.2$), thereby compressing the representation. The final stage is Linear($H/2 \rightarrow prediction$), which produces the scalar output. This *wide* \rightarrow *narrow* \rightarrow *scalar* design balances expressive power and regularization for downstream regression.

E.3 Training Strategies and Hyperparameter

E.3.1 Evaluation Protocol

The reported results are averaged over three independent runs. Statistical tests for the synthetic data are provided in Appendix G.4.3. To further assess robustness on the largest REST-meta-MDD dataset, we additionally adopt the leave-two-site-out evaluation protocol, which is commonly used in the medical domain. Detailed results for REST-meta-MDD are reported in Appendix G.2.

E.3.2 Data Preprocessing

Prior to training, all input features (both modalities) and targets are independently standardized to zero mean and unit variance using scikit-learn’s `StandardScaler`. For the synthetic data experiment, we generate a dataset of 10 000 samples following the prescribed formulation. The *Synthetic*, *CT Slice*, and *Superconductivity* datasets are each split into training, validation, and test sets using a fixed random seed. For *CMU-MOSI*, *CMU-MOSEI*, and *Vision&Touch*, we employ the official train/val/test partitions, while **Rest-meta-MDD** is divided by site.

E.3.3 Model Initialization & Latent Dimensions

We initialize all Linear and Conv layer weights using Kaiming initialization and set biases to zero [He et al., 2015]. For all experiments, the latent dimensions of Z_1 and Z_2 are set to 64 to provide sufficient representational capacity while controlling the computational overhead of PID decomposition.

E.3.4 Optimizer & Learning Rate Scheduling

We employ two Adam optimizers: one for the predictor and projection networks, and one for the information-bottleneck coefficient λ^b . A ReduceLROnPlateau scheduler is attached to the predictor optimizer, monitoring validation prediction loss with factor = 0.5, patience = 10 epochs, and min_lr = 10^{-6} . The initial learning rates are 1×10^{-3} for the predictor/projection optimizer and 0.1 for the λ optimizer.

E.3.5 Loss Weights

We empirically observe that setting $\lambda_1 = \lambda_2 = \lambda_3 = 0.1$ delivers consistently robust performance across all datasets; and each regularizer's contribution is confirmed by our ablation studies. We do not consider any additional performance gains from dataset-specific λ hyperparameter tuning to ensure concise and consistent.

E.3.6 Regularization & Gradient Management

Dropout (rates between 0.2 and 0.5) is interleaved with BatchNorm in all MLP layers. We apply L_2 -norm gradient clipping with a maximum norm of 1.0 to the predictor subnetwork.

E.3.7 Early Stopping & Checkpointing

Training is halted when the validation total loss fails to decrease for 30 consecutive epochs. Whenever the validation loss reaches a new minimum, we save the model weights, optimizer state, the λ^b parameter, and PID fusion weights. After training completes, the best checkpoint is reloaded for final test evaluation.

E.3.8 Batch Size & Memory Requirements

We use a batch size of 32 for **CMU-MOSI**, 20 for **Rest-meta-MDD**, and 256 for all other datasets. Experiments on **Rest-meta-MDD** require at least 24 GB of GPU memory (e.g., NVIDIA RTX 4090 or equivalent).

F Extension to Multivariate Gaussian and More than Two Modalities

Extending the PID framework to more than two input sources is a widely recognized open problem in information theory. Even with three sources, the complete Williams–Beer [Williams and Beer, 2010] lattice already comprises 18 distinct partial-information atoms that enumerate all unique, redundant, and synergistic interactions. the number of such atoms increases super-exponentially with the number of inputs. In what follows, we introduce a practical formulation for three modalities and outline two complementary optimization strategies, further highlighting the potential of PIDReg.

F.1 Pragmatic Simplification for Three Modalities

Given this combinatorial complexity, we can adopt a pragmatic simplification. Specifically, we aggregate all redundancy-related atoms into a single overall redundancy term, and similarly, group all synergy-related atoms into a single overall synergy term (please refer to Fig.1(b) in Griffith and Koch [2014]). This enables us to decompose the total mutual information $I(Z_1, Z_2, Z_3; Y)$ as:

$$I(Z_1, Z_2, Z_3; Y) = R + U_{Z_1} + U_{Z_2} + U_{Z_3} + S, \quad (43)$$

where R represents the common information redundantly available in all three sources, U_{Z_i} represents the information uniquely available in source Z_i , S captures all synergistic interactions that are only present when multiple sources are considered together.

In the meantime, we also have:

$$\begin{cases} I(Z_1; Y) = R + U_{Z_1} \\ I(Z_2; Y) = R + U_{Z_2} \\ I(Z_3; Y) = R + U_{Z_3} \end{cases} \quad (44)$$

However, Eqs. (43) and (44) involve five variables but only four equations, making the system underdetermined. To resolve this ambiguity, we formally specify the Union Information (the sum of all unique information and redundancy) as:

$$I^U := \min_{Q \in \Delta_P} I_Q(Z_1, Z_2, Z_3; Y). \quad (45)$$

Importantly, this aggregation not only alleviates the combinatorial complexity of the full PID lattice but also admits a natural optimization-based formulation, as elaborated in Appendix F.2.

F.2 Tractable Optimization Objective

The above definitions generalize the two-source definition from Venkatesh et al. [2023], Bertschinger et al. [2014]. In the special case where Z_1, Z_2, Z_3, Y are jointly Gaussian, the optimization defining union information and unique

information becomes particularly tractable. We take I^U as an example, since mutual information and conditional mutual information admit closed-form expressions over Gaussian variables, the optimization of I^U reduces to the following convex optimization over covariance matrices:

$$\min_{\Sigma_Q \succeq 0} I_{\Sigma_Q}(Z_1, Z_2, Z_3; Y) \quad \text{s.t. } \Sigma_Q^{Z_i, Y} = \Sigma_P^{Z_i, Y}, \quad i = 1, 2, 3, \quad (46)$$

where Σ_Q is the candidate joint covariance matrix, and $\Sigma_Q^{Z_i, Y}$ denotes its (X_i, Y) marginal block.

By definition:

$$I(Y; Z_1, Z_2, Z_3) = \frac{1}{2} \log \left(\frac{\det(\Sigma_{Z_1 Z_2 Z_3})}{\det(\Sigma_{Z_1 Z_2 Z_3|Y})} \right). \quad (47)$$

According to Venkatesh et al. [2023], the optimization problem can be reformulated as follows:

$$I^U := \min_{\Sigma_{Z_1 Z_2 Z_3|Y}} \frac{1}{2} \log \det \left(I + \sigma_Y^{-2} \begin{bmatrix} \Sigma_{Y Z_1}^P \\ \Sigma_{Y Z_2}^P \\ \Sigma_{Y Z_3}^P \end{bmatrix} \left(\Sigma_{Z_1 Z_2 Z_3|Y}^Q \right)^{-1} \begin{bmatrix} \Sigma_{Y Z_1}^P \\ \Sigma_{Y Z_2}^P \\ \Sigma_{Y Z_3}^P \end{bmatrix}^\top \right) \quad \text{s.t. } \Sigma_{Z_1 Z_2 Z_3|Y}^Q \succeq 0, \quad (48)$$

which has the same optimization form as Eq.(5) and is likewise amenable to projected gradient descent.

F.3 Gradients and Optimization

For compactness, denote:

$$M := I + \sigma_Y^{-2} \begin{bmatrix} \Sigma_{Y Z_1}^P \\ \Sigma_{Y Z_2}^P \\ \Sigma_{Y Z_3}^P \end{bmatrix} \left(\Sigma_{Z_1 Z_2 Z_3|Y}^Q \right)^{-1} \begin{bmatrix} \Sigma_{Y Z_1}^P \\ \Sigma_{Y Z_2}^P \\ \Sigma_{Y Z_3}^P \end{bmatrix}^\top, \quad f(\Sigma_{Z_1 Z_2 Z_3|Y}^Q) := \frac{1}{2} \log \det M. \quad (49)$$

The differential of f with respect to $\Sigma_{Z_1 Z_2 Z_3|Y}^Q$ is:

$$\begin{aligned} df &= \frac{1}{2} \text{tr}(M^{-1} dM) \\ &= -\frac{1}{2} \sigma_Y^{-2} \text{tr} \left(\left(\Sigma_{Z_1 Z_2 Z_3|Y}^Q \right)^{-1} \begin{bmatrix} \Sigma_{Y Z_1}^P \\ \Sigma_{Y Z_2}^P \\ \Sigma_{Y Z_3}^P \end{bmatrix}^\top M^{-1} \begin{bmatrix} \Sigma_{Y Z_1}^P \\ \Sigma_{Y Z_2}^P \\ \Sigma_{Y Z_3}^P \end{bmatrix} \left(\Sigma_{Z_1 Z_2 Z_3|Y}^Q \right)^{-1} d\Sigma_{Z_1 Z_2 Z_3|Y}^Q \right). \end{aligned} \quad (50)$$

Consequently,

$$\nabla_{\Sigma_{Z_1 Z_2 Z_3|Y}} f = -\frac{1}{2} \sigma_Y^{-2} \left(\Sigma_{Z_1 Z_2 Z_3|Y}^Q \right)^{-1} \begin{bmatrix} \Sigma_{Y Z_1}^P \\ \Sigma_{Y Z_2}^P \\ \Sigma_{Y Z_3}^P \end{bmatrix}^\top M^{-1} \begin{bmatrix} \Sigma_{Y Z_1}^P \\ \Sigma_{Y Z_2}^P \\ \Sigma_{Y Z_3}^P \end{bmatrix} \left(\Sigma_{Z_1 Z_2 Z_3|Y}^Q \right)^{-1}. \quad (51)$$

Starting from any feasible initialization $\Sigma_{Z_1 Z_2 Z_3|Y}^{Q(0)} \succeq 0$, we apply a projected gradient descent scheme:

$$\tilde{\Sigma}^{Q(t+1)} = \Sigma_{Z_1 Z_2 Z_3|Y}^{Q(t)} - \eta_t \nabla_{\Sigma_{Z_1 Z_2 Z_3|Y}} f \left(\Sigma_{Z_1 Z_2 Z_3|Y}^{Q(t)} \right), \quad \Sigma_{Z_1 Z_2 Z_3|Y}^{Q(t+1)} = \Pi_{\mathbb{S}_+} \left(\tilde{\Sigma}^{Q(t+1)} \right), \quad (52)$$

where $\eta_t > 0$ is the step size. The operator $\Pi_{\mathbb{S}_+}$ denotes the projection onto the cone of positive semi-definite (PSD) matrices, ensuring that the constraint $\Sigma^Q \succeq 0$ is preserved at every iteration. Specifically, if $X = U \text{diag}(\lambda_1, \dots, \lambda_d) U^\top$ is the eigendecomposition of X , then:

$$\Pi_{\mathbb{S}_+}(X) = U \text{diag} \left(\max\{\lambda_1, 0\}, \dots, \max\{\lambda_d, 0\} \right) U^\top + \varepsilon I, \quad (53)$$

with a small $\varepsilon > 0$ added as a safeguard for numerical stability. To select a suitable step size η_t , we adopt a backtracking line search based on the Armijo rule, which guarantees a sufficient decrease of the objective [Nocedal and Wright, 2006], i.e., $f(\Sigma^{Q(t+1)}) \leq f(\Sigma^{Q(t)})$. The iteration terminates once the progress becomes negligible, $|f(\Sigma^{Q(t+1)}) - f(\Sigma^{Q(t)})| < \delta$, or when a budget of steps is reached. For robustness, all matrix inverses in Eq. (51) are evaluated via linear solves, and $\log \det(\cdot)$ is computed using slogdet to avoid numerical overflow or underflow.

Synergy. With the optimizer $\Sigma_{Z_1 Z_2 Z_3 | Y}^{Q*}$ obtained by the projected gradient scheme in Eqs.(51) to(53), we derive the corresponding I^{U*} . Together with the total mutual information given by Eq. (47), the synergy component can then be expressed as:

$$S = I(Z_1, Z_2, Z_3; Y) - I^{U*}. \quad (54)$$

Redundancy. For each $i \in \{1, 2, 3\}$, the pairwise mutual information is computed directly from the empirical covariance Σ^P :

$$I(Z_i; Y) = \frac{1}{2} \log \det \left(I + \sigma_Y^{-2} \Sigma_{YZ_i}^P (\Sigma_{Z_i Z_i}^P)^{-1} \Sigma_{Z_i Y}^P \right). \quad (55)$$

Under the pragmatic three modality decomposition and the definition of union information for three modalities, we have:

$$I^U = R + U_{Z_1} + U_{Z_2} + U_{Z_3}, \quad I(Z_i; Y) = U_{Z_i} + R \quad (i = 1, 2, 3), \quad (56)$$

which leads to the following expression for redundancy:

$$R = \frac{I(Z_1; Y) + I(Z_2; Y) + I(Z_3; Y) - I^{U*}}{2}. \quad (57)$$

By substituting Eq.(55) into Eq.(57), the redundancy can be numerically evaluated.

Uniqueness. Each unique information term admits a closed-form expression:

$$U_{Z_i} = I(Z_i; Y) - R = I(Z_i; Y) - \frac{I(Z_1; Y) + I(Z_2; Y) + I(Z_3; Y) - I^{U*}}{2}, \quad i \in \{1, 2, 3\}. \quad (58)$$

F.4 Network Implementation

In terms of network implementation, we can introduce a new modality-specific encoder for X_3 to generate Z_3 . The final fused representation can then be formulated as:

$$Z = w_1 Z_1 + w_2 Z_2 + w_3 Z_3 + w_{123} (Z_1 \circ Z_2 \circ Z_3), \quad (59)$$

similar to Eq.(2), the last term explicitly captures the synergistic effect. The weights w_1, w_2, w_3 and w_{123} are adjusted by the computed PID terms accordingly.

F.5 Experimental Results of Tri-Modal PIDReg

We further evaluate on the **CMU-MOSI** and **CMU-MOSEI**, both of which are inherently tri-modal (text, audio, and video), comparing the tri-modal extension of PIDReg against its bi-modal counterpart. The predictive results are reported in Table 9, while the corresponding information decomposition is provided in Table 10.

Method	CMU-MOSI					CMU-MOSEI				
	A ₇ ↑	A ₂ ↑	F1 ↑	MAE ↓	Corr ↑	A ₇ ↑	A ₂ ↑	F1 ↑	MAE ↓	Corr ↑
PIDReg [♡]	32.0	80.0	79.7	0.938	0.662	47.4	80.2	80.0	0.634	0.662
PIDReg [♣]	37.2	80.8	80.9	0.947	0.664	47.0	80.6	80.2	0.642	0.661
PIDReg [△]	16.4	52.3	51.8	1.400	0.149	41.7	63.4	63.7	0.828	0.228
PIDReg [♦]	38.2	81.6	81.6	0.899	0.699	48.7	81.7	81.5	0.620	0.679

Table 9: Tri-Modal PIDReg results ([♣] denotes modality combination of Text–Vision–Audio).

Component	CMU-MOSI					CMU-MOSEI				
	U_1^Δ	U_2^\square	U_3°	R	S	U_1^Δ	U_2^\square	U_3°	R	S
Value	0.110	0.052	0.077	0.817	6.108	0.083	0.070	0.081	0.496	6.372

Table 10: Tri-modal Gaussian PID decomposition. Δ Text modality, \square Vision modality, \circ Audio modality.

It is noteworthy that the high synergy observed in Table 10 aligns with the inherent logic of multimodal sentiment prediction in **CMU-MOSI** and **CMU-MOSEI**. This further explains why the performance improvement from Table 2 to Table 9 primarily stems from the synergistic information across different modalities in predicting sentiment.

G Extended Results

G.1 Computational Efficiency

PIDReg introduces no additional trainable parameters compared to standard fusion models and therefore does not increase model complexity. The encoder and predictor networks follow conventional architectures (e.g., MLPs, ResNet), as detailed in Appendices E.1 and Appendix E.2. PIDReg performs one PID optimization per iteration in the first phase, slightly increasing training time, but remains comparable to other methods. Table 11 reports the average training time per epoch across representative baselines on same device (all require 200 epochs of training).

Method	DER	MoNIG	PIDReg
Time	1.756	3.280	4.641

Table 11: Average training time per epoch (in seconds).

G.2 Fine-Grained Results on Rest-meta-MDD

In Table 3 of the main paper, we present brain age regression results averaged across all sites. Detailed, site-specific performance metrics are reported in Table 12 (We have preserved the site-labeling conventions from Yan et al. [2019] and related works, no adjustments have been made). In brain-age prediction, models commonly exhibit a *regression-to-the-mean* effect—overestimating young subjects’ ages and underestimating older subjects’. To eliminate this systematic bias and thereby ensure that the corrected age estimates yield more reliable and interpretable outcomes, we first fit a simple linear model on the training set [Beheshti et al., 2019, Cole et al., 2017]:

$$\hat{y}_i = \alpha + \beta y_i + \varepsilon_i, \quad (60)$$

where y_i is the chronological age and \hat{y}_i the raw model prediction. The estimated intercept α and slope β quantify the overall offset and compression of the prediction relative to true age.

Any new prediction \hat{y}^{raw} is then bias-corrected via:

$$\hat{y}^{\text{corr}} = \frac{\hat{y}^{\text{raw}} - \alpha}{\beta}, \quad (61)$$

so that, by construction, $\hat{y}^{\text{corr}} \approx y$ lies on the identity line within the training distribution [Smith et al., 2019]. Equivalently, one may report the residual brain-age gap:

$$\Delta_i = \hat{y}_i^{\text{raw}} - (\alpha + \beta y_i), \quad (62)$$

which is inherently uncorrelated with chronological age.

To avoid information leakage, this correction is performed independently. The resulting age-adjusted predictions (or brain-age gaps) are thus independent of true age, enhancing both interpretability and the validity of downstream associations with biological or clinical variables.

Fig. 7 further provides an intuitive visual summary of PIDReg’s raw versus linear bias-corrected age predictions across all sites.

Test Site(s)	Age	Gender(M/F)	Sample(MDD/HC)	MV		MIB		MoNIG		NIG		CoMM		PIDReg	
				MAE	Corr	MAE	Corr	MAE	Corr	MAE	Corr	MAE	Corr	MAE	Corr
S20	39.0 ± 13.9	157/322	250/229	7.900	0.794	9.048	0.608	7.960	0.792	7.498	0.628	7.749	0.592	7.518	0.797
S7,S9	33.5 ± 11.4	79/89	83/85	9.497	0.479	6.374	0.679	9.591	0.379	10.619	0.107	10.187	-0.131	7.776	0.723
S14,S19	31.7 ± 8.4	53/89	79/63	6.793	0.824	5.103	0.633	8.232	0.611	8.912	0.579	10.438	-0.037	4.284	0.751
S1,S8	31.7 ± 9.2	106/156	127/135	7.946	0.592	6.696	0.513	9.223	0.426	9.855	0.364	9.574	0.253	5.967	0.687
S17,S10	26.5 ± 9.0	65/88	86/67	7.292	0.637	5.757	0.739	6.610	0.785	6.872	0.773	7.316	0.675	4.687	0.776
S23,S15	37.5 ± 14.3	44/68	52/60	7.759	0.764	7.727	0.708	9.454	0.761	17.693	0.771	11.375	0.357	6.678	0.849
S22,S13	31.1 ± 9.8	34/40	38/36	10.123	0.334	8.476	0.448	11.250	0.525	9.901	0.456	8.476	0.373	6.553	0.562
S21,S11	34.3 ± 11.9	79/102	99/82	7.959	0.622	7.039	0.657	9.894	0.446	11.932	0.313	9.825	0.373	7.977	0.754
S2,S4	35.7 ± 11.1	24/47	34/37	5.196	0.847	4.556	0.790	6.130	0.580	6.931	0.825	10.229	-0.034	5.172	0.843

Table 12: Cross-site results on Rest-meta-MDD.

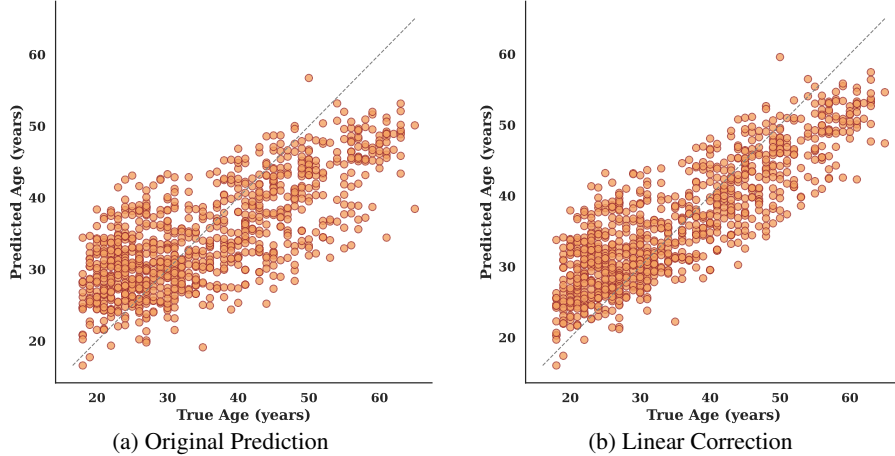


Figure 7: Brain age prediction results.

G.3 Large Scale Bimodal MNIST Regression Benchmark

Given the scarcity of large-scale, high-quality benchmarks for bimodal regression with known information contributions, we additionally design a new benchmark derived from the MNIST dataset. Specifically, starting from the 70,000 grayscale images of size 28×28 , we construct a dataset of 140,000 samples as follows:

For each original image, sample a rotation angle $\theta \sim \mathcal{U}(-90^\circ, 90^\circ)$, which serves as the regression target. Rotate the image by θ degrees, add Gaussian noise whose standard deviation is drawn from $\mathcal{U}(0, 0.05)$, and apply a random contrast scaling sampled from $\mathcal{U}(0.8, 1.2)$. For each augmented image, we extract two heterogeneous feature modalities:

Raw - pixel modality: Flatten the 28×28 image into a 784-dimensional vector X_1 , preserving all low-level visual information.

Structured - feature modality: Concatenate four classes of handcrafted descriptors, statistical moments, edge and gradient features, shape-contour descriptors, and frequency-domain features, into a 278-dimensional vector X_2 , aimed at capturing higher-order structural information.

Each sample is thus associated with a scalar target θ and two modalities $X_1 \in \mathbb{R}^{784}$ and $X_2 \in \mathbb{R}^{278}$. We then compare PIDReg against baseline methods in terms of predictive performance and information decomposition. The results are reported in Table 13.

Metric	MIB	MoNIG	MEIB	DER	PIDReg	Component	U_1^*	U_2°	R	S
MAE↓	7.70	9.28	10.17	10.01	5.90	Value	0.866	0.000	0.250	0.076
$R^2 \uparrow$	0.95	0.94	0.86	0.91	0.97					

Table 13: MNIST regression (left) and Gaussian PID decomposition values (right), *Pixel modality, $^\circ$ Feature modality.

The raw-pixel modality retains the complete visual content of each image. Because the structured-feature modality is derived solely from descriptors that encode the same rotation-angle information present in the raw pixels, it does not contribute substantial additional information. The PID decomposition therefore unambiguously reveals the intrinsic

relationship between these two modalities (redundant and no unique information from X_2). The results on MNIST further underscore the effectiveness and robustness of PIDReg on real world data.

G.4 Evaluation of PIDReg under Extreme Scenarios and Gaussian Distribution Shifts

To further validate the superiority of PIDReg in terms of predictive accuracy and information decomposition, we conduct additional experiments from two perspectives: (i) extreme boundary cases of information components (section G.4.1), and (ii) severely skewed non-Gaussian information components (section G.4.2). All results are further subjected to statistical tests in section G.4.3 to rule out potential confounding effects.

G.4.1 Extreme Scenarios Extension

First, we follow the same setup as in section 4.1, where synthetic data are generated according to Eq.(22) and Eq.(23). Here, however, we additionally consider cases with purely single information components. We repeat the experiments under this setting, and the results, shown in Fig. 8, demonstrate that PIDReg can still accurately capture the information components even in such extreme cases.

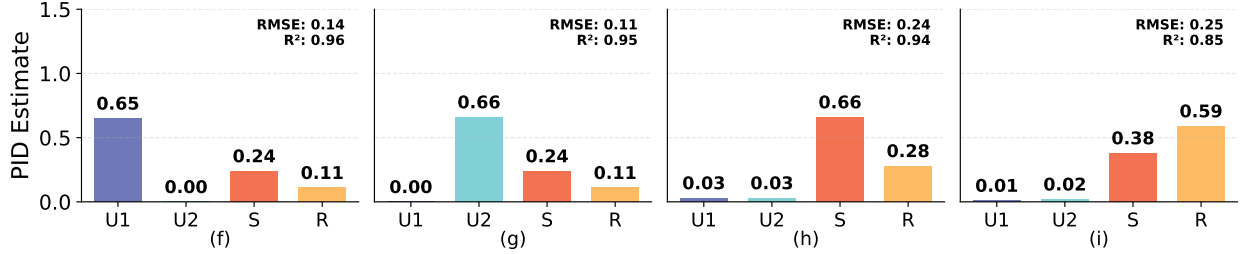


Figure 8: Estimated PID values when (f) $w_{u1} = 1.00$, $w_{u2} = 0.00$, $w_s = 0.00$, $w_r = 0.00$; (g) $w_{u1} = 0.00$, $w_{u2} = 1.00$, $w_s = 0.00$, $w_r = 0.00$; (h) $w_{u1} = 0.00$, $w_{u2} = 0.00$, $w_s = 1.00$, $w_r = 0.00$; (i) $w_{u1} = 0.00$, $w_{u2} = 0.00$, $w_s = 0.00$, $w_r = 1.00$.

G.4.2 Gaussian Distribution Shifts

Furthermore, instead of drawing $R, U_1, U_2 \sim \mathcal{N}(0, 1)$, we sample them from a chi-squared distribution, $R, U_1, U_2 \sim \chi_4^2$, such that the variables significantly deviate from Gaussianity, the results are shown in Fig. 9. This allows us to provide an additional validation of PIDReg from the perspective of known ground truth, thereby assessing its reliability under skewed data distributions that often arise in real-world scenarios.

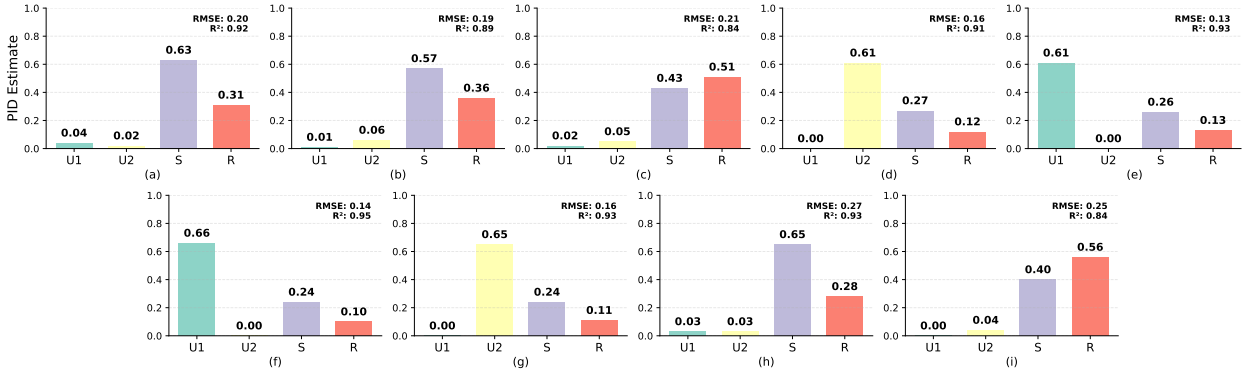


Figure 9: Estimated PID values when (a) $w_{u1} = 0.00$, $w_{u2} = 0.00$, $w_s = 0.75$, $w_r = 0.25$; (b) $w_{u1} = 0.00$, $w_{u2} = 0.00$, $w_s = 0.50$, $w_r = 0.50$; (c) $w_{u1} = 0.00$, $w_{u2} = 0.00$, $w_s = 0.25$, $w_r = 0.75$; (d) $w_{u1} = 0.00$, $w_{u2} = 0.80$, $w_s = 0.10$, $w_r = 0.10$; (e) $w_{u1} = 0.80$, $w_{u2} = 0.00$, $w_s = 0.10$, $w_r = 0.10$; (f) $w_{u1} = 1.00$, $w_{u2} = 0.00$, $w_s = 0.00$, $w_r = 0.00$; (g) $w_{u1} = 0.00$, $w_{u2} = 1.00$, $w_s = 0.00$, $w_r = 0.00$; (h) $w_{u1} = 0.00$, $w_{u2} = 0.00$, $w_s = 1.00$, $w_r = 0.00$; (i) $w_{u1} = 0.00$, $w_{u2} = 0.00$, $w_s = 0.00$, $w_r = 1.00$.

Furthermore, we retain the experimental protocol and apply the scalable procedure of Liang et al. [2023], which quantifies interaction information for datasets or pre-trained models. In contrast to PIDReg's **intrinsic interpretability**

(built-in, training-time decomposition), Liang et al. [2023] is a **post-hoc diagnostic**. We replicate the experiments and compute the resulting information-decomposition estimates, with outcomes summarized in Fig. 10. Notably, under severely skewed, non-Gaussian distributions, the post-hoc method exhibits limited ability to capture the dynamics of information components.

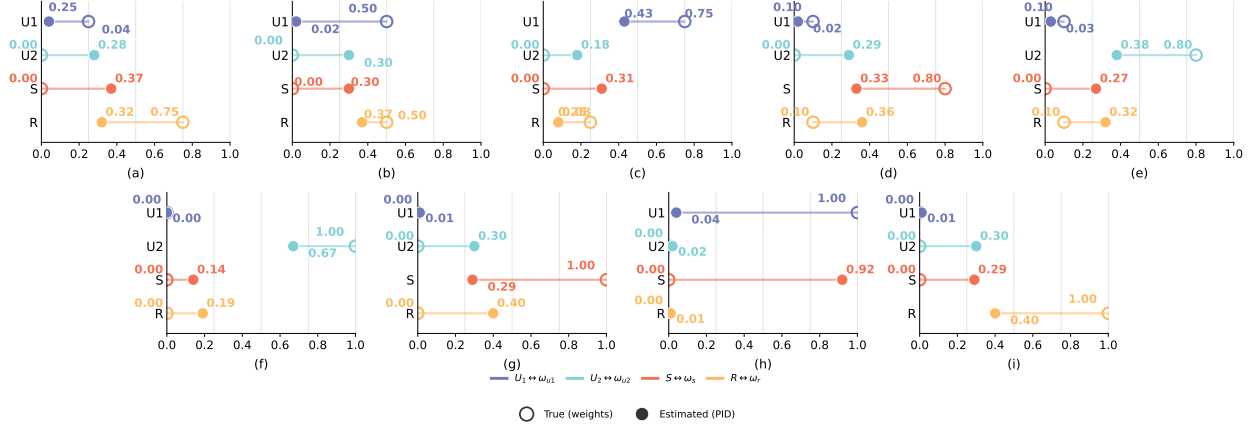


Figure 10: Post-hoc diagnostic estimated PID values.

G.4.3 Statistical Test

We further employ statistical tests to examine the significance of PIDReg in capturing and decomposing information components. Specifically, we validate the estimation of ω_R/ω_S by fixing $\omega_{u1} = \omega_{u2} = 0.2$ and varying $\omega_R/\omega_S \in \{0, 0.5, 1, 1.5, 2.0\}$, with 10 trials conducted for each ratio. The Pearson correlation between the ground-truth ratio and the estimated $R_{\text{est}}/S_{\text{est}}$ yields:

$$r = 0.996, \quad p = 3.02 \times 10^{-4} < 0.05,$$

demonstrating a significant positive correlation and confirming the reliability of PIDReg’s decomposition capability.

Remark 1 (Interpretation of estimated PID components). *The true weights $\omega_{u1}, \omega_{u2}, \omega_R, \omega_S$ and the estimated PID components U_1, U_2, R, S differ in both their physical units and the mathematical spaces they inhabit, so numerical discrepancies are expected. In Eq.(23), $\omega_{u1}, \omega_{u2}, \omega_R, \omega_S$ are linear scaling factors applied to latent variables in the generative process. For example, modality 1 follows:*

$$X_1 = f_{\text{gen}}([R, U_1]), \quad Z_1 = h_{\phi_1}(X_1),$$

so that ω modulates the composite function $h_{\phi_1} \circ f_{\text{gen}}$. This makes the true contributions of unique information and redundancy highly nonlinear, and the estimated components U_1, U_2, R, S capture the resulting influence after such transformations. Hence, exact numerical consistency with the original linear weights is not expected.

Nevertheless, we design our experiments to test whether the estimated PID components reliably reflect the relative strengths of the underlying generative factors, which we expect to be positively correlated with the true weights. The results in Fig. 2, Fig. 8 and Fig. 9 confirm two main objectives:

1. **Detection of information — channel existence.** When a generative channel is switched off, the model should detect its absence, e.g.,

$$\omega_{u1} = 0 \implies U_1 \approx 0.$$

2. **Trend tracking of relative contributions.** When the relative strengths of information components change, the estimated PID components should reflect the correct monotonic trend, e.g.,

$$w_s^{(2)} > w_s^{(1)}, \quad w_r^{(2)} < w_r^{(1)} \implies S_{\text{est}}^{(2)} > S_{\text{est}}^{(1)}, \quad R_{\text{est}}^{(2)} < R_{\text{est}}^{(1)}.$$

H Limitations and Future Work

The current PIDReg framework provides modality-level or dataset-level interpretability by revealing how different higher-order modality interactions contribute to the final prediction. For future work, we aim to extend this capability toward sample-level (instance-level) interpretability. In this setting, when making inference for a specific sample, PIDReg would be able to identify the most informative unique modality or modality interaction that drives the prediction.